submitted to *Geophys. J. Int.*

Full wave sensitivity of $SK(K)S$ phases to arbitrary anisotropy in the upper and lower mantle

Andrea Tesoniero[1], Kuangdai Leng[1,2], Maureen Long[1], Tarje Nissen-Meyer[2]

[1] *Department of Geology and Geophysics, Yale University, 210 Whitney Avenue, New Haven, (CT),* 06520*, USA*

[2] *Department of Earth Sciences, University of Oxford, South Parks Road, Oxford OX1 3AN, UK*

14 March 2020

SUMMARY

Core-refracted phases such as SKS and $SKKS$ are commonly used to probe seismic anisotropy in the upper and lowermost portions of the Earth's mantle. Measurements of $SK(K)S$ splitting are often interpreted in the context of ray theory, and their frequency dependent sensitivity to anisotropy remains imperfectly understood, particularly for anisotropy in the lowermost mantle. The goal of this work is to obtain constraints on the frequency dependent sensitivity of $SK(K)S$ phases to mantle anisotropy, particularly at the base of the mantle, through global wavefield simulations. We present results from a new numerical approach to modeling the effects of seismic anisotropy of arbitrary geometry on seismic wave propagation in global 3D Earth models using the spectral element solver AxiSEM3D. While previous versions of AxiSEM3D were capable of handling radially anisotropic input models, here we take advantage of the ability of the solver to handle the full fourth-order elasticity tensor, with 21 independent coefficients. We take advantage of the computational efficiency of the method to compute wavefields at the relatively short periods ($5s$) that are needed to simulate $SK(K)S$ phases. We benchmark the code for simple, single-layer anisotropic models by measuring the splitting (via both the splitting intensity and the traditional splitting parameters ϕ and δt) of synthetic waveforms and comparing them to well-understood analytical solutions. We then carry out a series of numerical experiments for laterally homogeneous upper mantle anisotropic

models with different symmetry classes, and compare the splitting of synthetic waveforms to predictions from ray theory. We next investigate the full wave sensitivity of $SK(K)S$ phases to lowermost mantle anisotropy, using elasticity models based on crystallographic preferred orientation of bridgmanite and post-perovskite. We find that $SK(K)S$ phases have significant sensitivity to anisotropy at the base of the mantle, and while ray theoretical approximations capture the first-order aspects of the splitting behavior, full wavefield simulations will allow for more accurate modeling of $SK(K)S$ splitting data, particularly in the presence of lateral heterogeneity. Lastly, we present a cross-verification test of AxiSEM3D against the SPECFEM3D_GLOBE spectral element solver for global seismic waves in an anisotropic Earth model that includes both radial and azimuthal anisotropy. A nearly perfect agreement is achieved, with a significantly lower computational cost for AxiSEM3D. Our results highlight the capability of AxiSEM3D to handle arbitrary anisotropy geometries and its potential for future studies aimed at unraveling the details of anisotropy at the base of the mantle.

Key words: Elasticity Tensor – Numerical Simulation – Spectral Element Method – Anisotropy – Lower Mantle – Wave Propagation

1 INTRODUCTION

Seismic anisotropy, the property of elastic materials to manifest directionally dependent seismic wave speeds (e.g., Anderson, 1989; Babuska & Cara, 1991), occurs in many regions of the Earth, including the crust (e.g., Barruol & Kern, 1996), the upper mantle (e.g., Silver, 1996; Savage, 1999), the transition zone (e.g., Foley & Long, 2011; Yuan & Beghein, 2013), the uppermost lower mantle (e.g., Lynner & Long, 2015; Ferreira et al., 2019), the D'' region at the base of the mantle (e.g., Nowacki et al., 2011; Creasy et al., 2017), and the inner core (e.g., Beghein & Trampert, 2003). Because mantle anisotropy reflects deformation processes, knowledge of its presence, style, and strength yields insight into past and present mantle flow (e.g., Long & Becker, 2010). The proper characterization of seismic anisotropy is therefore crucial for our understanding of the dynamics of Earth's mantle. Our ability to completely characterize anisotropy in the mantle is limited, however, in part due to limitations imposed by seismic data coverage, and in part due to theoretical or computational limitations to relate observations to Earth structure. It is common in many global seismological studies to either neglect anisotropy entirely, and consider an isotropic approximation to Earth structure, or to consider only simple anisotropic geometries, such as radial anisotropy.

Elastic anisotropy manifests itself in the seismic wavefield in many ways, including the difference in propagation velocity between vertically polarized Rayleigh waves and horizontally polarized Love waves (e.g., Anderson, 1961; Moulik & Ekström, 2014), the splitting of normal modes (e.g., Anderson & Dziewonski, 1982; Tromp, 1995; Beghein et al., 2008), the directional dependence of travel times of body waves such as P_n (e.g., Hess, 1964; Buehler & Shearer, 2017) or surface waves (e.g Forsyth, 1975; Schaeffer et al., 2016), the scattering of energy from Love waves to Rayleigh waves via the coupling of spheroidal and toroidal modes (e.g., Park & Yu, 1993; Servali et al., 2020), the polarization of P waves (e.g., Schulte-Pelkum et al., 2001), and directionally dependent P-to-S conversions as manifested in receiver functions (e.g., Levin & Park, 1998; Wirth & Long, 2014). The most widely used technique for detecting anisotropy in the mantle, however, is shear wave splitting or birefringence (e.g., Silver, 1996; Savage, 1999; Long & Silver, 2009). The splitting of SKS and $SKKS$ phases is routinely measured to study anisotropy in both the

upper mantle (e.g., Silver & Chan, 1991; Wolfe & Silver, 1998; Levin et al., 1999; Long & van der Hilst, 2005; Long, 2013; Roy et al., 2014) and in the lowermost mantle (e.g., Niu & Perez, 2004; Restivo & Helffrich, 2006; Long, 2009; Long & Lynner, 2015; Roy et al., 2014; Grund & Ritter, 2018; Reiss et al., 2019). Core traversing phases such as SKS and $SKKS$ have several distinct advantages for shear wave splitting analysis. These include the known initial polarization of the shear wave, controlled by the P to S conversion at the core-mantle boundary (CMB), the lack of source-side effects, and the ability to observe clear $SK(K)S$ phases that are often easily identifiable on seismograms. Shear wave splitting analysis also has several shortcomings, however; chief among these is the lack of vertical resolution of anisotropy, since it is a path-integrated measurement, and the need to obtain splitting measurements from multiple azimuths in order to fully characterize the anisotropic structure.

While a full 21 elastic parameters are needed to fully describe arbitrary anisotropy, it is common to use simpler parameterizations of anisotropy that invoke assumptions about anisotropic symmetry. For example, in global tomographic inversions that include radial anisotropy, under the assumption of hexagonal symmetry (e.g., Auer et al., 2014; Tesoniero et al., 2015), it is typical to use 5 parameters to describe the model, rather than the 2 needed for the isotropic case (e.g., Ritsema et al., 2011). Similarly, inversions of SKS splitting data for azimuthal anisotropy in the upper mantle typically rely on reduced parameterizations (e.g., Monteiller & Chevrot, 2011; Lin et al., 2014a; Mondal & Long, 2019). While such parameterizations may make sense in the context of practical limitations on observational data sets, they may not always be realistic for actual Earth materials. For example, olivine, the primary mineral constituent of the upper mantle and the major cause of upper mantle anisotropy, has orthorhombic symmetry, although deformed olivine aggregates may be approximated with higher symmetry classes (e.g., Karato et al., 2008). In any case, it is desirable to have computational tools that can simulate accurate wave propagation through anisotropic media of arbitrary symmetry efficiently; furthermore, azimuthal anisotropy is a well-known property of the upper mantle, so it is necessary for wavefield modeling schemes to be able to handle azimuthal anisotropy in addition to the more commonly invoked radial anisotropy.

Measurements of shear wave splitting are commonly interpreted in the framework of ray the-

ory, either implicitly or explicitly. The most straightforward interpretation of SKS splitting measurements, for example, invokes a single layer of azimuthal anisotropy beneath a station whose properties (symmetry axis orientation, strength of anisotropy, and/or layer thickness) are related to the observed splitting parameters (typically fast splitting direction, ϕ and delay time, δt) via a simple ray theoretical approximation. In some cases, complex patterns of SKS splitting, in which apparent splitting parameters vary with backazimuth, are interpreted as reflecting multiple layers of anisotropy (e.g., Marson-Pidgeon & Savage, 2004; Eakin & Long, 2013), via analytical equations that were developed based on a ray theoretical approximation (Silver & Savage, 1994). While there has been some work on the nature of the frequency dependent sensitivity of SKS phases to upper mantle anisotropy (e.g., Favier & Chevrot, 2003; Favier et al., 2004; Chevrot, 2006; Long et al., 2008; Sieminski et al., 2008; Lin et al., 2014a; Mondal & Long, 2019), only a few observational studies have actually used finite-frequency sensitivity estimates to interpret (or invert) actual data (Monteiller & Chevrot, 2011; Lin et al., 2014b). Furthermore, the finite-frequency sensitivity of SKS and $SKKS$ phases to anisotropy in the lowermost mantle remains poorly understood. Given the increasing use of $SK(K)S$ phases in studies of deep mantle anisotropy, it is crucial to understand the nature of this sensitivity.

For both upper and lowermost mantle anisotropy studies, it is desirable to have a computationally efficient tool to simulate global seismic wave propagation for $SK(K)S$ phases in anisotropic media with arbitrary symmetry. The popular spectral-element based community software package SPECFEM3D_GLOBE (Komatitsch & Tromp, 2002a,b) is capable of handling arbitrary anisotropy, but its significant computational requirements make global simulations at the periods relevant for $SK(K)S$ phases (down to $\sim 5-10s$) impractical. In this study, we make use of the AxiSEM3D code (Leng et al., 2016, 2019), a coupled pseudo-spectral spectral element solver for 3D global wavefield propagation in realistic 3D Earth models. While previously released versions of AxiSEM3D only handled radially anisotropic input models, the actual solver is capable of handling the full fourth-order elasticity tensor C_{ijkl} with 21 independent coefficients. We have modified the formulation of the input models to handle arbitrary elasticity, and in this study we test and implement a range of anisotropic mantle models that include azimuthal anisotropy, relevant for $SK(K)S$ split-

ting. The AxiSEM3D code combines the advantages of a full 3D spectral element method to model complex, 3D structures with the computational efficiency of axi-symmetric methods; this allows the user to model complex and realistic Earth structures with significant computational speedup and without significant loss of performance (Leng et al., 2019).

The goal of this study is to evaluate the frequency dependent effects of anisotropy of different symmetry classes (albeit in relatively simple, laterally homogeneous structures) on the splitting of $SK(K)S$ phases, via global wavefield simulations for seismic periods down $5s$. We generate synthetic seismograms for a suite of Earth models with anisotropy in the upper and lowermost mantle, and analyze the synthetic SKS and $SKKS$ waveforms by measuring shear wave splitting using both the traditional transverse component energy minimization method (Silver & Chan, 1988) and the splitting intensity method (Chevrot, 2000). We present benchmark results for simple cases, including one based on the spherically symmetric PREM model (Dziewonski & Anderson, 1981) and one that invokes vertically propagating shear waves traveling through a transverse isotropic medium with a horizontal axis of symmetry (HTI). We then model global wave propagation for more realistic upper mantle anisotropy scenarios, including approximations to olivine crystallographic preferred orientation (CPO) that invoke both hexagonal and orthorhombic symmetry. Next, we investigate the effects of anisotropy in the D'' layer at the base of the mantle on $SK(K)S$ splitting, via a series of global wavefield simulations for models that invoke CPO of lower mantle minerals such as bridgmanite and post-perovskite. In the last part we provide a verification of our implementation of full anisotropy via a benchmark solution against the full 3D spectral element solver SPECFEM3D_GLOBE. We then discuss the implications of our results from relatively simple models for future work on the interpretation of shear wave splitting measurements in terms of mantle anisotropy, particularly as more complex models are considered.

2 ANISOTROPIC MODELING STRATEGY WITH AXISEM3D

AxiSEM3D (Leng et al., 2016, 2019) is a powerful hybrid spectral element solver for 3D global wave propagation in realistic Earth structures. It aims to bridge the gap between computationally expensive simulation methods for 3D Earth structure and faster simulation methods for spheri-

cally symmetric Earth models. It is a fully convergent 3D method not unlike other discrete full 3D methods e.g. SPECFEM3D_GLOBE. The method follows the axi-symmetric spectral element solver AxiSEM which assumes spherically symmetric or axi-symmetric structures. To accommodate arbitrary 3D structures, AxiSEM3D is built upon a collection of coupled axi-symmetric 2D domains. This relies on the fact that wavefields in realistic 3D structures are relatively smooth in the azimuthal direction (Leng et al., 2016), and can thus be accurately represented in the azimuthal direction by honoring this smooth complexity rather than a complexity-blind, fine discretization just as in the in-plane dimension or for conventional 3D methods. AxiSEM3D couples the azimuthal dimension by Fourier series, which can assume arbitrarily low or high expansion orders for each patch in the source-receiver plane. This hybrid formulation combines the strength of a full 3D discrete method to compute global wavefields with the significant speedup of computational time of 2D methods. In other words, a 3D global wavefield in complex Earth models can be efficiently computed at a cost that scales almost as (multiple) 2D simulations, allowing us to run simulations of global wavefield propagation over a large frequency range with relatively limited computer resources. This computational efficiency is coupled with the capability of AxiSEM3D to readily allow the usage of 3D Earth models based on global tomography, including those available from the Incorporated Research Institutions for Seismology (IRIS) Earth Model Collaboration (EMC) in netCDF format. Independent modules can be invoked to handle certain geometrical properties, such as surface topography or topography on boundaries such as the CMB (Leng et al., 2019). AxiSEM3D automatically handles radial anisotropy if the velocity structure of the underlying seismic velocity model is provided as horizontal and vertical compressional and shear wave velocity values. Detailed descriptions of the theoretical formulation of AxiSEM3D and benchmark tests with independent, fully 3D discrete spectral element solvers (e.g. SPECFEM3D_GLOBE) are given in (Leng et al., 2016, 2019).

For this study, we take advantage of the accuracy and efficiency of the method to solve the elastodynamic wave equation in global media, and implement a new independent module which introduces general anisotropy of arbitrary symmetry. The mathematical formulation of the three-dimensional wave equation is based on the generalized Hooke's law, $\sigma_{ij} = C_{ijkl}\varepsilon_{kl}$,which relates

the components of the stress tensor σ_{ij} to the strain tensor ε_{kl} through the fourth-order elasticity tensor C_{ijkl}. The elasticity tensor describes the elastic properties of the material, and in the most general case it can be fully described by 21 independent coefficients (see Malvern, 1969; Babuska & Cara, 1991, for details). In the new anisotropic module, the elastic properties of a specific anisotropic region in the domain are described by 21 independent elastic parameters, as opposed to the 2 Lamé constants (λ and μ) for the isotropic case or the 5 Love parameters (A, C, L, N, F, described further below) for the vertical transverse isotropy (VTI) case. In order to use the general anisotropy module in AxiSEM3D, the user must provide the solver with a netCDF file containing the information about the elasticity tensor and the anisotropic media's geographical location within the model domain.

Introducing general anisotropy (an intrinsically 3D property of the medium) usually only accounts for a relatively small increment of the total computational cost. However, similarly to the case for lateral heterogeneity in (isotropic) velocity structure, the user must ensure that the Fourier degree of expansion is larger than the size of the heterogeneous structure, in order to ensure a correct representation of the seismic wavefield. Moreover, the user must take particular caution in taking into account the geometrical properties of the elasticity tensor. This is usually defined in a local coordinate system such that certain crystallographic axes (or a strain directions) align certain geographic coordinates. However, AxiSEM3D works with a global spherical coordinate system. Therefore, except at the geographical poles (where the coordinate systems coincide), a rotation matrix must be applied to the elasticity tensor (specified by the user in a local coordinate system) to translate its orientation to the global domain of AxiSEM3D.

3 BENCHMARK TESTS FOR SIMPLE ANISOTROPIC MODELS

We begin by running two different numerical tests with the intention to benchmark the new anisotropic module of AxiSEM3D against well-understood wave propagation behavior for simple anisotropic models. In the first of these, we run a global wavefield simulation for the 1D PREM model (Dziewonski & Anderson, 1981), which includes radial anisotropy in the depth range between $25km$ and $220km$ depth. In the second of these, we run wave propagation simulations for a

simple, single layer of anisotropy with a horizontal axis of transverse isotropy (HTI), reproducing a synthetic test presented in Chevrot (2000).

3.1 Radially anisotropic PREM

In the first test, we run global wavefield simulations for PREM under two different conditions: (1) using the traditional model input format of AxiSEM3D, in which radial anisotropy is specified via horizontal and vertical velocity values for both P and S waves, and (2) using the model input format of the new anisotropy module, in which anisotropy is specified via the full elasticity tensor. This allows us to test whether we have correctly implemented the specification of elasticity in the new module, and whether we have correctly implemented the tensor rotations needed to map the local coordinate system of the model input file to the global spherical coordinate system of AxiSEM3D. In order to parameterize the PREM model in the new input file, we replace the elastic constants in the depth range between $24km$ and $220km$ with equivalent elastic coefficients of the 6×6 elasticity tensor that describes the radial anisotropy contained in anisotropic PREM. At other depths, we use the isotropic PREM values, which are specified via the Lamé constants λ, μ (and the density ρ). The relationship between the full elasticity tensor C_{ijkl} and the Love parameters that describe radial anisotropy are given by the following relationships (e.g., Babuska & Cara, 1991):

$$
\begin{aligned}
A &= \rho {V_{PH}}^2 \\
C &= \rho {V_{PV}}^2 \\
L &= \rho {V_{SV}}^2 \\
N &= \rho {V_{SH}}^2 \\
F &= \eta(A - 2L)
\end{aligned}
\tag{1}
$$

$$C_{ijkl} = \begin{pmatrix} A & A-2N & F & \cdot & \cdot & \cdot \\ A-2N & A & F & \cdot & \cdot & \cdot \\ F & F & C & \cdot & \cdot & \cdot \\ \cdot & \cdot & \cdot & L & \cdot & \cdot \\ \cdot & \cdot & \cdot & \cdot & L & \cdot \\ \cdot & \cdot & \cdot & \cdot & \cdot & N \end{pmatrix} \quad (2)$$

with A, C, L, N being the parameters associated to the horizontal and vertical compressional and shear seismic wavespeed and F being the parameter associated to seismic waves propagating in intermediate directions through the coefficient η. We run the simulation for a hypothetical earthquake in the South American subduction zone whose moment tensor is represented by the focal mechanism in Figure 1, which also shows the two sets of synthetic seismograms for different components at three representative stations (FFC, GRFO, and COCO). This test shows the general ability of our new anisotropy module to correctly specify the full elasticity tensor for models that include radial anisotropy; however, this test is not capable of capturing the effects that azimuthally dependent anisotropy have on the propagating wavefield.

3.2 Single anisotropic layer with vertical wave propagation

In order to test whether the new anisotropy model correctly represents the effects of azimuthal anisotropy for simple models, we carry out a second benchmarking exercise modeled on a synthetic test presented in Chevrot (2000). We consider wave propagation through a single layer of anisotropy of thickness $30km$, with a horizontal axis of transversely isotropic symmetry (HTI) at an azimuth of 45° North. The strength of anisotropy in the layer is 3%, and the value of the parameter η is 1.03. We use a density of $2450kg/m^3$ along with an average P wave velocity of $6.50km/s$ and an S wave velocity of $3.75km/s$ for the anisotropic layer. In order to mimic the synthetic test of Chevrot (2000) closely, and to avoid global waveform effects, we use a point source sitting directly beneath the receiver, just beneath the anisotropic layer to induce perfectly vertical S wave propagation. We use a monopole point source that radiates energy entirely polarized in a single direction, and consider different polarization directions of the source in order to explore the

azimuthal dependence of the waveforms. To properly define the backazimuth, we set both source and receiver located along the same vertical direction, with the source slightly shifted along the latitudinal direction by $0.01°$. This minor deviation does not substantially affect the polarization of the seismic energy which will remain confined in a single direction. As an alternative approach, we also tested a scheme that keeps source and receiver perfectly assigned and instead rotates the elasticity tensor by $15°$ for each simulation. Both approaches deliver the same results. We designate the horizontal component parallel to the initial polarization direction of the S wave as the radial component, and examine how the behavior of the transverse component varies with azimuth (following Chevrot (2000)). We convolve the synthetic seismograms with a Gaussian source-time function with half-duration of $5s$, which corresponds to the resolution period of the mesh used for this simulation.

Radial and transverse component seismograms as a function of backazimuth for this simulation are shown in Figure 2, which demonstrates the expected behavior of the transverse component waveform for azimuthal anisotropy (Vinnik et al., 1989; Chevrot, 2000). While the radial component does not change much with azimuth, the transverse component is azimuthally dependent, and its shape takes the form of the time derivative of the radial component, multiplied by a scalar factor that depends on the angle between the initial polarization of the shear wave and the azimuth of the fast symmetry axis (as well as the strength of anisotropy). We observe the expected behavior of no energy on the transverse component in the case where the initial polarization is parallel or perpendicular to the fast axis orientation (Figure 2), and a maximum in transverse component energy when the initial polarization is $45°$ from the symmetry axis. Following equations (7) and (A4) from Chevrot (2000), we measure the splitting intensity for each synthetic seismogram, which is defined as:

$$SI = -2\frac{T(t)R'(t)}{\|R'(t)\|^2} \tag{3}$$

The splitting intensity measured as a function of backazimuth forms the splitting intensity vector which is shown in Figure 3. Estimates of the splitting parameters (ϕ δt) can be derived from fitting a $\sin(2\theta)$ curve to the splitting intensity vector shown in Figure 3, using the relationship

$SI \simeq -1/2\delta t \sin 2(\beta)$, where β corresponds to the angle between the initial polarization direction and the azimuth of the fast symmetry axis. Our estimates of the splitting parameters derived from Figure 3 are $\phi = 45°$ and $\delta t = 0.228s$, which agree well with the values for the same test in Chevrot (2000).

4 UPPER MANTLE ANISOTROPY SIMULATIONS AND COMPARISON WITH RAY THEORY

4.1 Background: Upper mantle anisotropy and shear wave splitting

Seismic anisotropy in the upper mantle is generally interpreted in terms of the CPO of anisotropic upper mantle minerals, primarily olivine. The relationships between strain and the resulting CPO are complex and depend on many factors, potentially including stress, temperature, pressure, water content, deformation history, and preexisting fabric (e.g., Karato et al., 2008; Skemer & Hansen, 2016). Despite these complications, however, a number of simplified relationships are often used to interpret $SK(K)S$ splitting data, often with implicit assumptions made about the symmetry of the anisotropic medium. For example, upper mantle anisotropy is often modeled using a hexagonal approximation to the actual elastic tensor (e.g., Browaeys & Chevrot, 2004; Becker et al., 2006), even though olivine itself is orthorhombic, and even though actual aggregates of mantle rocks may have even lower symmetry in practice. As discussed in the Introduction, the interpretation of $SK(K)S$ data is usually done in the context of ray theory, with only a few exceptions. While a few studies have examined the finite-frequency sensitivity of $SK(K)S$ splitting to upper mantle anisotropy (e.g., Favier & Chevrot, 2003; Favier et al., 2004; Chevrot, 2006; Long et al., 2008; Sieminski et al., 2008; Zhao & Chevrot, 2011; Lin et al., 2014a), it is relatively uncommon to carry out global wavefield simulations to model the effects of upper mantle anisotropy on $SK(K)S$ splitting. The purpose of the tests presented in this section is to establish the new anisotropy module of AxiSEM3D as a viable tool for doing so, and to explore how anisotropy models of increasing complexity in terms of their symmetry (from hexagonal to orthorhombic) affect $SK(K)S$ waveforms.

A second goal of these tests is to understand to what extent shear wave splitting measurements

performed on synthetic seismograms derived from global wavefield simulations depart from the predictions of ray theory. Work by Lin et al. (2014a) established that full-wavefield effects on $SK(K)S$ phases can cause significant deviations from ray theoretical predictions of shear wave splitting, even for relatively simple (laterally homogenous) upper mantle anisotropy models. We aim to extend our understanding of this phenomenon here, particularly as it relates to the interpretation of $SKS - SKKS$ splitting discrepancies. Relatively large discrepancies between the splitting of SKS and $SKKS$ phases for the same event-station pair are typically interpreted as evidence for a contribution to the splitting of one or both phases from anisotropy in the lower mantle (e.g., Niu & Perez, 2004; Long, 2009; Lynner & Long, 2014; Grund & Ritter, 2018; Reiss et al., 2019). However, Lin et al. (2014a) showed that wavefield effects that depart from the predictions of ray theory can cause small discrepancies in splitting intensity values (up to $\sim 0.3s$) between SKS and $SKKS$ phases for models that only include upper mantle anisotropy. The work of Lin et al. (2014a) used computations of finite-frequency sensitivity kernels based on the formulation of Zhao & Chevrot (2011). Here we build on this work using a complementary method (global wavefield simulations as opposed to explicit sensitivity kernel computations).

In order to compare the splitting of synthetic $SK(K)S$ waveforms to the predictions of ray theory (and eventually to real data), we measure both the splitting intensity introduced by Chevrot (2000), as described in section 3.2, and the traditional splitting parameters (ϕ, δt) using the transverse component minimization method of Silver & Chan (1991). We use the implementation of the Silver & Chan (1991) method in **SplitRacer** (Reiss & Rümpker, 2017), a MATLAB-based graphical user interface for teleseismic shear wave splitting analysis. We compare the splitting measurements made on synthetic waveforms with predictions from ray theory, derived from the Python tool **christoffel** (Jaeken & Cottenier, 2016), which solves the Christoffel equation to predict the polarizations and velocities of the quasi-S phases for waves propagating over a range of directions.

4.2 Upper mantle case #1: Horizontal transverse isotropy (HTI)

We now introduce a global wavefield simulation for a case that includes azimuthal anisotropy, in the form of a (single, laterally homogenous) anisotropic layer in the upper mantle with HTI symmetry. We do this simply by modifying the radially anisotropic upper mantle layer in PREM from a VTI symmetry to an HTI symmetry by rotating the symmetry axis by $90°$. The symmetry axis thus lies in the horizontal plane for this simulation. The properties of the anisotropic layer are shown visually in Figure 4, which shows representations of the anisotropic properties of various scenarios tested in this paper. The VTI elastic tensor of PREM is represented in Figure 4, top row, while the rotated HTI tensor used in this test is shown in Figure 4, second row. In order to avoid waveform complexity due to structural heterogeneity, we use a laterally homogeneous, 1D Earth model that corresponds to PREM except for in the depth range between $24km$ and $220km$, where we impose the HTI elastic tensor described above. We neglect attenuation and ellipticity in the simulation, even though this can be simulated with AxiSEM3D in general. We use a source and receiver configuration shown in the left panel of Figure 5, with the source located at the surface (to avoid depth phases resulting from reflections off the free surface). The receiver is located at the North Pole, while the sources are located at $15°$ azimuthal intervals at an epicentral distance of $120°$, at which both SKS and $SKKS$ phases should be visible (e.g., Long, 2009). The moment tensor for each source is chosen to maximize the radiation of S wave energy in the direction of the receiver, as shown in Figure 5. While our simulations reproduce the entire wavefield, we focus on the portions of the synthetic seismograms that show the SKS, $SKKS$, and S_{diff} phases; the ray-theoretical paths of these phases are shown in the right panel of Figure 5. The synthetic seismograms for the radial and transverse components plotted against the backazimuthal direction of the incoming wavefield are shown in Figure 6 in a time-window that includes SKS, $SKKS$, and S_{diff} phases. We also show synthetic waveforms as a function of backazimuth for epicentral distances of $100°$ and $110°$ in the Supplementary Information (Figures S1-S2).

The splitting analysis results of this simulation are shown in Figure 7, which shows the measured splitting intensity as a function of backazimuth from the synthetic seismograms for SKS and $SKKS$ phases, along with the predictions from ray theory. The ray theoretical predictions

were obtained by solving the Christoffel equation for an elasticity tensor that was averaged over the depth range of the anisotropic layer, with the SKS and $SKKS$ propagation directions derived from **TauP** (Crotwell et al., 1999) for the PREM model. As expected, the measured splitting intensity values exhibit a variation with backazimuth that is close, but not identical, to that predicted by ray theory (solid orange and dashed red curves in Figure 7). The full wavefield solution yields splitting intensity values that are systematically smaller, by up to $\sim 0.25s$, than the ray theoretical predicted values. Similar to Lin et al. (2014b), we also find modest differences in SKS and $SKKS$ splitting intensity, of up to $\sim 0.2s$, at certain azimuths, with the difference being largest at a backazimuth that is 30° from the fast direction. We retrieve the best-fitting splitting parameters $(\phi, \delta t)$ for SKS and $SKKS$, respectively, by fitting a $sin(2\theta)$ curve to the splitting intensity measurements in Figure 7, and obtain values of $\phi = 90^\circ$ and $\delta t = 0.780s$ for SKS and $\phi = 90^\circ$ and $\delta t = 0.862s$ for $SKKS$. These values generally compare well to the ray theoretical values of $\delta t = 1.036s$ for SKS and $\delta t = 1.038s$ for $SKKS$, although again, ray theory overpredicts the amplitude of the splitting compared to the wavefield simulations. Finally, we compare the splitting parameters obtained from the splitting intensity curve to those obtained by the transverse component minimization method at two representative backazimuths, shown in Figure 8. As with the splitting intensity measurements, there are modest differences in measured splitting parameters between SKS and $SKKS$ phases at the same backazimuth, although in this case these differences are not significant considering the error estimates (Figure 8).

4.3 Upper mantle case #2: Orthorhombic symmetry

We now explore a case in which the upper mantle anisotropic layer has a lower symmetry class. Because CPO of olivine is generally understood to be the main cause of upper mantle anisotropy, and because single-crystal olivine has an orthorhombic symmetry, it is reasonable to test an orthorhombic model. Single-crystal olivine has a strong anisotropy, up to $\sim 25\%$ for P waves and $\sim 22\%$ for S waves, according to laboratory measurements (Babuska & Cara, 1991; Isaak, 1992; Abramson et al., 1997; Mao et al., 2015). The bulk anisotropy in deformed olivine aggregates, however, is significantly lower than the single-crystal anisotropy (e.g., Ben Ismaïl & Mainprice,

1998; Karato et al., 2008). We constructed a model for upper mantle anisotropy by taking an averaging approach that preserves the symmetry class of the orthorhombic single crystal but decreases its anisotropy strength. We used the **MSAT** code (Walker & Wookey, 2012) to calculate a linear mixture consisting of 30% San Carlos single-crystal olivine at upper mantle conditions, as described by Abramson et al. (1997), and 70% isotropic PREM. The resulting elasticity tensor (Figure 4, third row) has a similar symmetry of a single crystal of olivine (we choose an orientation such that the [100] and [001] axes are in the horizontal direction, and the [010] axis is oriented vertically), but the anisotropy is substantially weaker ($\sim 5\%$ maximum). As in the HTI upper mantle simulation, the anisotropic layer is confined between $24km$ and $220km$ depth.

We show the results of our wavefield simulation in Figure 9, which is similar to Figure 7 but for the orthorhombic symmetry case. Synthetic seismograms across a range of backazimuths at epicentral distances of 100° , 110°, and 120° for this simulation are shown in the Supplementary Information (Figures S3-S5). Because of the departure from hexagonal symmetry, the ray theoretical predictions (solid orange and dashed red lines in Figure 9) are no longer perfect $\sin(2\theta)$ curves, and in this case ray theory predicts some discrepancies between SKS and $SKKS$ phases at certain azimuths. The measured splitting intensity values from the synthetic seismograms show some departures from the ray theoretical predictions, as in the HTI simulation, but for the orthorhombic case the departures are more pronounced (compare Figure 9 with Figure 7). As with the HTI case, there are a few azimuths for which we find discrepancies in $SKS - SKKS$ splitting intensities; somewhat surprisingly, this discrepancy is quite large (difference in splitting intensity of $\sim 0.4s$) at backazimuths that lie 45° away from the fast splitting direction. An examination of the transverse component minimization measurements at selected backazimuths (Figure 10) shows that the $SKKS$ splitting measurement at a backazimuth of 45° is poorly constrained due to a stronger interference of a not well identifiable phase on the radial component that leads to the contamination of the splitting measurements.

5 LOWERMOST MANTLE ANISOTROPY SIMULATIONS AND COMPARISON WITH RAY THEORY

5.1 Background: Lowermost mantle anisotropy and shear wave splitting

We now turn our attention to seismic anisotropy in the lowermost mantle, which has been the subject of a great deal of recent observational work (e.g., Wookey et al., 2005a; Long, 2009; Nowacki et al., 2010; Cottaar & Romanowicz, 2013; Lynner & Long, 2014; Ford et al., 2015; Creasy et al., 2017; Grund & Ritter, 2018; Reiss et al., 2019), but which is substantially more challenging to observe than upper mantle anisotropy. As summarized in Nowacki et al. (2011) and Creasy et al. (2019), there are a variety of possible mechanisms that may contribute to anisotropy in the D'' layer, including CPO of bridgmanite or post-perovskite (depending on which mineral dominates, which may in turn depend on the temperature in a given region of D'' (Houser, 2007)), CPO of ferropericlase, or shape-preferred orientation (SPO) of elastically distinct material such as partial melt. We do not test all of these possible mechanisms in this paper; instead, we test models of aligned post-perovskite and aligned bridgmanite, one of which is expected to be the most volumetrically important phase in any given region of D''. Testing of other models for D'' anisotropy will be left to future work.

There are a variety of strategies for measuring D'' anisotropy using body waves, only some of which rely on $SK(K)S$ phases. One common approach is to measure the differential splitting of $S - ScS$ phases (introduced by Wookey et al. (2005a); see also Wookey & Kendall (2008); Ford et al. (2015); Rao et al. (2017)) or to examine the waveform behavior of phases such as S_{diff} (e.g., Cottaar & Romanowicz, 2013). The identification of significant discrepancies between the splitting of SKS and $SKKS$ phases for the same event-station pair, first documented by James & Assumpção (1996), have been attributed to anisotropy at the base of the mantle beginning with Niu & Perez (2004) and Restivo & Helffrich (2006). The measurement of $SKS-SKKS$ splitting discrepancies to study D'' anisotropy is becoming more common (e.g., Long, 2009; He & Long, 2011; Roy et al., 2014; Lynner & Long, 2014, 2015; Grund & Ritter, 2018), although there is some debate about the extent to which $SKS - SKKS$ splitting discrepancies require a contribu-

tion to the lowermost mantle. Some studies (Monteiller & Chevrot, 2011; Lin et al., 2014a) have argued that $SKS-SKKS$ splitting discrepancies can be explained solely in terms of upper mantle anisotropy. Recently, some studies of $SKS-SKKS$ splitting discrepancies have come to rely on the measurement of splitting intensity, rather than the traditional splitting parameter estimation methods, on the grounds that the splitting intensity is a more robust and stable measurement (Deng et al., 2017; Reiss et al., 2019). Despite ample observational evidence that $SK(K)S$ phases can indeed be affected by anisotropy in the lowermost mantle, there is still no consensus in the literature about how strong the finite-frequency sensitivity of these phases is to anisotropy in D'' (Sieminski et al., 2008; Zhao & Chevrot, 2011). Furthermore, there are disagreements in the literature about to what extent documented $SKS-SKKS$ splitting discrepancies reflect a contribution to splitting from lowermost mantle anisotropy to one or both phases (e.g., Niu & Perez, 2004; Restivo & Helffrich, 2006; Long, 2009), or whether such discrepancies can mainly be attributed to upper mantle anisotropy (e.g., Monteiller & Chevrot, 2011; Lin et al., 2014a). There is, therefore, a need for global wavefield simulations that include lower mantle anisotropy.

Another argument for the study of full-wave effects of D'' anisotropy on $SK(K)S$ phases comes from recent work that has sought to carry out forward modeling of D'' anisotropy, relying on results from mineral physics (e.g., Walker et al., 2011; Cottaar et al., 2014; Ford et al., 2015; Ford & Long, 2015; Creasy et al., 2017, 2019; Walker et al., 2018; Tommasi et al., 2018). These types of modeling studies tend to rely exclusively on ray theory, with very few exceptions (e.g., Nowacki & Wookey (2016), who looked at full-wave effects for complex anisotropic models but who only considered ScS phases). Given the popularity of these types of modeling approaches, it is crucial to understand how well the ray theoretical approximation captures the true behavior of $SK(K)S$ waves.

5.2 Lowermost mantle case #1: Bridgmanite crystallographic preferred orientation

We first consider a case that invokes a laterally homogeneous, $250km$ thick D'' layer at the base of the mantle, with elasticity that is designed to capture the first-order characteristics of aligned bridgmanite. Because the dominant slip systems at lowermost mantle conditions remain uncertain,

we follow the strategy of recent modeling studies (e.g., Ford et al., 2015; Creasy et al., 2017) and consider tensors based on single-crystal elasticity. We chose an orientation such that the [100] and [010] axes of bridgmanite are oriented in the horizontal direction, while the [001] axis is vertical. We create an elastic tensor via a linear mixture of 30% single crystal anisotropy of post-perovskite, using the elastic constants from Wookey et al. (2005b), with 70% of isotropic PREM at D'' depths. This mixing ratio yields an elastic tensor with an orthorhombic symmetry and with a maximum anisotropy of 6%, as shown in Figure 4, fourth row. As with the upper mantle cases, we propagate the seismic wavefield through this model using the source and receiver geometries shown in Figure 5, and measure the splitting intensity, as well as the traditional shear wave splitting parameters, as a function of backazimuth. Also as with the upper mantle cases, we compare the synthetic splitting measurements with predictions from ray theory. In contrast to the upper mantle case, in the lowermost mantle the SKS and $SKKS$ phases under study have significantly different ray propagation paths. Using **TauP** (Crotwell et al., 1999), we calculated nominal propagation angles (from the horizontal) through the D'' region of $67°$ for SKS and $42°$ for $SKKS$.

Results from our bridgmanite simulation are shown in Figures 11 and 12. Synthetic seismograms across a range of backazimuths at epicentral distances of $100°$, $110°$, and $120°$ for this simulation are shown in the Supplementary Information (Figures S6-S8). Because the raypaths of SKS and $SKKS$ phases depart so significantly from the vertical, we no longer expect a simple $\sin 2(\theta)$ variability in the splitting intensity curve, and this is borne out by the measurements on synthetic seismograms. For this reason, we do not fit a $\sin 2(\theta)$ curve to our measurements, as we did for the upper mantle cases. We do predict the ray theoretical splitting intensity curves, as shown on Figure 11; these are based on the predicted apparent splitting parameters at each azimuth, visualized in Figure 4, fourth row. As with the upper mantle cases, particularly the HTI simulation, we find that the full-wavefield simulations predict splitting intensity behavior that is generally similar to the ray theoretical predictions, but not identical to it. We see deviations of up to $\sim 0.2s$ in splitting intensity values between the ray theoretical predictions and the synthetic seismogram measurements at certain azimuths, again similar to what is observed for the upper mantle cases. Importantly, the bridgmanite model predicts spitting intensities of up to $\sim 0.8s$ for SKS

and $SKKS$ phases, nearly as large as the maximum values predicted from ray theory, indicating that these phases have significant sensitivity to anisotropy at the base of the mantle. Notably, both the synthetic seismogram measurements and the ray theoretical predictions indicate that at certain azimuths, significant discrepancies between SKS and $SKKS$ splitting intensities are expected, even though the underlying model is laterally homogeneous.

5.3 Lowermost mantle case #2: Post-perovskite crystallographic preferred orientation

Finally, we test a model that invokes aligned post-perovskite as the cause for D'' anisotropy. The phase transition from bridgmanite to post-perovskite, which was discovered experimentally by Murakami et al. (2004), is thought to be the cause of the D'' discontinuity, and is expected to dominate in relatively cold regions of the lowermost mantle (e.g., Hernlund et al., 2005), and perhaps throughout (e.g., Koelemeijer et al., 2018). Post-perovskite is generally favored as the most likely mechanism for D'' anisotropy by many authors (e.g., Nowacki et al., 2010; Walker et al., 2011; Cottaar et al., 2014; Ford et al., 2015). Similar to our test for bridgmanite, we create an elastic tensor that is a linear mixture of 30% single crystal anisotropy, using elastic constants for post-perovskite from Wookey et al. (2005b), and 70% isotropic PREM. In this scenario, we assume that the [100] and [010] axes are oriented in the horizontal directions, while the [001] axis is vertical. Predicted ray theoretical splitting patterns for this tensor are shown in Figure 4, bottom row.

Results from our post-perovskite wavefield simulation, along with ray theoretical predictions for this scenario at the relevant azimuths, are shown in Figure 13, and Figure 14 shows representative transverse component minimization splitting measurements at two azimuths. Synthetic seismograms across a range of backazimuths at epicentral distances of $100°$, $110°$, and $120°$ for this simulation are shown in the Supplementary Information (Figures S9-S11). Interestingly, for this orientation of the post-perovskite elasticity tensor, SKS phases are split only very weakly, with maximum splitting intensities of $\sim 0.2s$. This is consistent with the ray theoretical prediction for SKS splitting behavior (Figure 13; see also Figure 4, bottom row). The behavior of $SKKS$ phases provides a striking contrast; for the propagation angles relevant for $SKKS$, this elastic

tensor scenario predicts strong splitting, with maximum splitting intensities of $\sim 2.5s$. The azimuthal variation in the $SKKS$ splitting intensities measured from the synthetic seismograms is to first order captured by the ray theoretical prediction (Figure 13), although the synthetic splitting intensities are generally lower (sometimes by as much as $\sim 1.0s$) than the values predicted by ray theory. For the traditional splitting measurements (Figure 14), the splitting of SKS phases is so slight that there is not enough transverse component energy to obtain a stable measurement; as expected, these measurements do not yield meaningful splitting parameter estimates. For the $SKKS$ phases, in contrast, the transverse component minimization method yields robust measurements with strong splitting, consistent with the splitting intensity measurements (Figure 13) and as predicted by ray theory.

6 CROSS-VERIFICATION AGAINST AN INDEPENDENT 3D SPECTRAL ELEMENT SOLVER

Here we present a verification of our implementation of full anisotropy in AxiSEM3D by a benchmark solution against SPECFEM3D_GLOBE (Komatitsch & Tromp, 2002a,b). It is important to point out that the following benchmark test should be regarded as a cross-verification rather than a validation per se, as SPECFEM3D_GLOBE has not yet been benchmarked for global wavefield propagation in arbitrary anisotropic Earth models. We use the global-scale 3D anisotropic model of Montagner (2002), based on surface wave tomography, which includes both radial and azimuthal anisotropy. This model spans between the Moho (24km) and the 670km discontinuity and has a 5° horizontal resolution. Its elasticity tensor is determined by 13 independent parameters, numerically implemented as a fully anisotropic tensor with 21 independent parameters in both SPECFEM3D_GLOBE and AxiSEM3D. The benchmark problem, shown in Figure 15, is based upon simulating an earthquake source located in Virginia at a depth of $12km$, corresponding to the 2011 $Mw = 5.8$ earthquake in Mineral, VA. The source time function is an error function with half-duration of 10s. The synthetic seismograms are computed at 129 stations of the Global Seismographic Network (GSN) distributed across the Earth's surface (Figure 15). Attenuation is

turned off and the record length of the seismogram is 3600s. A nearly perfect agreement has been achieved between SPECFEM3D_GLOBE and AxiSEM3D in this simulation.

In Figure 16, we show the vertical components of a set of synthetic seismograms for stations (blue triangles in Figure 15) in the $\sim 90^\circ - 130^\circ$ range of epicentral distance. In this set of synthetic traces, which show a range of body wave arrivals as well as surface waves, the SPECFEM3D_GLOBE and AxiSEM3D traces are virtually indistinguishable. For reference, we also show corresponding synthetic seismograms computed for the radially anisotropic PREM, demonstrating the effect of the anisotropic structure in the Montagner (2002) model on the waveforms. Because the Montagner (2002) model only includes structure in the upper mantle, the major differences with PREM manifest in the upper mantle phases (SS, SSS) and the surface waves.

In Figure 17, we show the same set of synthetics, but we zoom in on the time window shown in Figure 16, to highlight the SKS and $SKKS$ arrivals. We show both radial (top panel) and transverse (bottom panel) component records; the latter shows the effect of azimuthal anisotropy in the Montagner (2002) model. The same version of this figure for the vertical component is shown in the Supplementary Information (Figure S12). For the transverse component traces in Figure 17 (bottom panel), the PREM model predicts no energy associated with the SKS or $SKKS$ time window; because PREM does not include azimuthal anisotropy, no splitting of $SK(K)S$ phases is predicted. The SPECFEM3D_GLOBE and AxiSEM3D synthetics, in contrast, show significant transverse component $SK(K)S$ energy at several of the selected stations. Again, the SPECFEM3D_GLOBE and AxiSEM3D traces are virtually indistinguishable in the time windows associated with $SK(K)S$ arrival. We also report in the Supplementary Information the full record section for the radial, transverse and vertical component of the all the stations localized in the $\sim 90^\circ - 130^\circ$ range of epicentral distance (Figures S13-S15). We do note some extremely small differences on the transverse components between the SPECFEM3D_GLOBE and AxiSEM3D traces in PS and PPS phases at some stations (e.g. II.MSVF). These differences are not visible on the corresponding radial components. These small differences are due to the fact that in general, phases with small amplitudes are more vulnerable to numerical errors (such as floating point errors

and discretisation errors). Because the two different methods have entirely different discretisation schemes, some small differences for low-amplitude phases are expected.

Compared to a fully discretised 3D method such as SPECFEM3D_GLOBE, AxiSEM3D has only one more parameter: the Fourier expansion order of the solution n_u (Leng et al., 2016, 2019). This parameter controls both the accuracy and the computational cost of AxiSEM3D. For a spherically symmetric Earth model such as PREM, we have $n_u = 2$ everywhere in the 2D computational domain of AxiSEM3D; in this case, AxiSEM3D degenerates to a pure axisymmetric spectral element method (Nissen-Meyer et al., 2014). For a 3D model, the AxiSEM3D solution converges to the real 3D solution as n_u increases, and its value for solution convergence is always much smaller (usually by orders of magnitude) than a fully-discretised one for global wave propagation in a realistic 3D Earth models (Leng et al., 2016). It is most efficient to vary n_u with depth and epicentral distance to maximise the performance of AxiSEM3D. Convergence tests are common practise in AxiSEM3D and are thoroughly explained in Leng et al. (2016, 2019). We refer the reader to (e.g., Leng et al., 2016, Fig.11) and to figure S16 in the Supplementary Information for a visual illustration of the convergence behaviour. In order to achieve the agreement demonstrated in Figures 16 with SPECFEM3D_GLOBE, we have used $n_u = 400$ in the uppermost $200km$ and $n_u = 100$ elsewhere. We enlarge n_u near the surface to have better accuracy for surface wave propagation. Such n_u field leads to highly-accurate waveforms for all the phases at all the stations in Figure 15. In terms of computer performance, with this n_u field, we have obtained a speedup of ~ 6 compared to SPECFEM3D_GLOBE. This speedup can be further increased in case neither surface waves nor multiple bouncing body waves (SSS, $SSSS$) are of interest. The technique of wavefield scanning (Leng et al., 2019) can be used to fully optimise n_u for better performance.

A key aspect of AxiSEM3D is its ability to correctly account for off great-circle scattering at minimal computational cost, via the Fourier expansion approach. This capability has been extensively discussed in previous papers (Leng et al., 2016, 2019), which include previous benchmark tests of the AxiSEM3D code against SPECFEM3D_GLOBE. Because the Montagner (2002) model involves strong upper mantle heterogeneity, and thus causes strong scattering from out-of-

plane structure, the benchmark test presented here provides a clear demonstration of the ability of AxiSEM3D to capture the complex properties of scattering by anisotropic heterogeneities in 3D.

7 DISCUSSION

7.1 A tool for efficient global wavefield modeling in arbitrary anisotropic media

The series of benchmark tests and global wavefield simulations presented in this paper establishes the AxiSEM3D code as an efficient tool for modeling of the global wavefield in Earth models that include anisotropy with arbitrary symmetry. In contrast to other 3D wavefield simulation methods, AxiSEM3D simulations can be run at periods that are relevant for studies of $SK(K)S$ splitting (down to $\sim 5 - 10s$ period) at relatively modest computational cost due to the sparse sampling of smoothness in the azimuthal wavefield. For example, the computational requirements for the global simulations presented in this paper involved about 3 hours and 30 minutes (wall-clock time) on 40 cores to produce $2000s$ long synthetic seismograms that can resolve seismic periods of $5s$.

The benchmarking tests presented in section 3 serve to validate the implementation of arbitrary anisotropy in AxiSEM3D. In the first case, we ran a global simulation for the PREM model, including radial anisotropy, in two ways: one in which the model was specified in terms of vertical and horizontal wave velocities in the anisotropic layer, and one in which the same model was specified in terms of the equivalent full elastic tensor C_{ijkl}. The two solutions were found to be numerically identical, as expected. In the second test, we replicated a synthetic test presented in Chevrot (2000) that included azimuthal anisotropy. This test successfully demonstrated the azimuthal dependence of transverse component waveforms, with the expected waveform shape, and reproduced the expected splitting parameters (as measured via the splitting intensity) found by Chevrot (2000) for this model case. The simulations for upper and lowermost mantle anisotropy presented in sections 4 and 5 demonstrate the feasibility of interrogating wavefield behavior due to anisotropy effects in the context of global models using AxiSEM3D, and the cross-validation tests with SPECFEM3D_GLOBE presented in section 6 yield a remarkable agreement between the two solutions, with a significant computational advantage obtained by AxiSEM3D.

7.2 Full wave sensitivity of $SK(K)S$ phases to upper and lowermost mantle anisotropy

The upper mantle anisotropy models presented here build on previous work on the finite-frequency sensitivity of $SK(K)S$ phases to azimuthal anisotropy in the upper mantle by a number of authors (e.g., Favier & Chevrot, 2003; Favier et al., 2004; Lin et al., 2014a; Mondal & Long, 2019) using a different set of tools (global wavefield simulations rather than sensitivity kernel computations). Similar to previous workers, we have found here that for laterally homogeneous models, ray theoretical approximations to the effects of upper mantle anisotropy on $SK(K)S$ splitting are generally accurate to first order. However, similar to Lin et al. (2014a), we also found that at certain azimuths and epicentral distance ranges, full waveform effects can produce modest deviations from the predictions of ray theory. Unlike Lin et al. (2014a), we examined models in our study with orthorhombic symmetry (in addition to transversely isotropic models) and found that the deviations from ray theoretical predictions are more pronounced at certain azimuths for this symmetry class.

There are several potential reasons for the (generally relatively minor) deviations between the synthetic splitting results and the ray theoretical predictions for our upper mantle models. The most important one is that AxiSEM3D considers full wave sensitivity to Earth structure and accounts for finite frequency effects, in contrast to ray theoretical methods. Other effects may include the fact that the ray theoretical calculations are based on a geometrical approximation of the path of the seismic ray traveling through an average, depth-weighted elasticity tensor; in AxiSEM3D, the elasticity is discretized in 33 different layers and varies with depth. Finally, like Lin et al. (2014a,b) we also noticed some complexities in the apparent splitting parameters due to interference with other seismic phases that could perturb the splitting measurement. This phenomenon is particularly recognizable in the HTI case, where a second wiggle is very close to the $SKKS$ phase, especially in the $30-60^\circ$ ($120-150^\circ$) backazimuthal ranges (Figure 6) and it can also be observed in the upper mantle orthorombic case at 45° (Figure 10). These other seismic phases coming in between SKS and $SKKS$ correspond to $PPPP$ phases: it can be observed from the seismograms directly that this phase is not split (no energy on the transverse component), consistent with it being a P phase.

The amplitude of this phase is strongly attenuated in real data seismograms, but since attenuation is turned off in our simulations they show up with high amplitude in our synthetics.

In general, while ray theory is generally an adequate approximation for $SK(K)S$ splitting due to upper mantle anisotropy, it is more likely to be inadequate when the anisotropic models under study are complicated (either in terms of their symmetry, as in this study, or when there are lateral variations in anisotropic structure, which was not considered here but which will be considered in future works). Similar to Lin et al. (2014a), we found that modest differences in splitting intensity for SKS vs. $SKKS$ phases (up to $\sim 0.2s$, with values up to $\sim 0.4s$ for specific symmetries and at certain azimuths) for the same event-station pair can be caused by waveform effects for models that include upper mantle anisotropy only. We note, however, that the $SKS - SKKS$ discrepancies due to upper mantle anisotropy documented in this study are modest compared to the larger discrepancies observed for the lowermost mantle cases (Section 5). For example, for the bridgmanite case, discrepancies larger than $0.5s$ and up to $\sim 1s$ are observed in the $30^\circ - 75^\circ$ ($105^\circ - 135^\circ$) backazimuthal range (Figure 11), while discrepancies as high as $\sim 2.5s$ are obtained for post-perovskite models (Figure 13). Our findings reinforce the need for $SKS - SKKS$ discrepancy studies of mantle anisotropy to exercise caution when interpreting weakly discrepant splitting, and to only attribute strong differences in splitting intensity values to anisotropy in the lowermost mantle (e.g., Deng et al., 2017; Reiss et al., 2019).

For the lower mantle, our results have shown that lowermost mantle anisotropy does have a significant effect on the splitting of SKS and $SKKS$ phases, in agreement with the sensitivity kernel computations of Zhao & Chevrot (2011) but in contrast to the suggestion of Sieminski et al. (2008) that $SK(K)S$ phases may have limited sensitivity to anisotropy in the lower mantle. A comparison between our shear wave splitting measurements on synthetic waveforms and the predictions of ray theory (for models that represent bridgmanite and post-perovskite elasticity) reveals that, as for the upper mantle models, ray theory generally correctly captures the first-order aspects of the splitting behavior. However, ray theory typically slightly overpredicts the magnitude of shear wave splitting when compared to the behavior of the full waveform. From these results, we conclude that forward modeling approaches for lowermost mantle anisotropy models that rely

on ray theory (e.g., Walker et al., 2011; Cottaar et al., 2014; Ford et al., 2015; Ford & Long, 2015; Creasy et al., 2017, 2019; Tommasi et al., 2018) are generally valid, but are less accurate than full-wavefield simulations. This implies that moving to approaches that consider the full waveform behavior is desirable in future modeling work aimed at D'' anisotropy problems, as also suggested by Nowacki & Wookey (2016).

7.3 Limitations and future work

While this study has established the feasibility of full-wave solutions using AxiSEM3D for Earth models that include anisotropy of arbitrary symmetry, it is important to highlight some caveats and limitations. One area in which particular concern must be taken in future studies of mantle anisotropy has to do with the design of the mesh and the size of anisotropic regions. In spectral element methods, the domain is subdivided into a number of non-overlapping quadrangular shaped elements, and on each element the nodes are chosen to be the Gauss-Lobatto-Legendre (GLL) points where the wave equation is evaluated (Peter et al., 2011). A good mesh design must consider this characteristic and allow for seismic discontinuities to lie on the GLL points. This will make sure that the points at the discontinuity have the elastic properties of both materials, which in turn will allow for the correct partitioning of seismic energy at the interface and avoid contamination of the numerical solution by artifacts due to staircase sampling effects. A proper mesh design is an essential requirement for all spectral element methods and not just AxiSEM3D. It is indeed a more complex task to achieve for 3D discrete methods as 3D meshes that honor these conditions have to be generated, while for AxiSEM3D this condition applies to 2D meshes. With this in mind, in future studies that interrogate anisotropic Earth models, it will be important to ensure that anisotropic discontinuities are also honored by the mesh design. This is relatively easy to accomplish in the case of vertical stratification of anisotropy (that is, horizontal interfaces), but it turns out to be more complex for cases of lateral variation in anisotropic properties, which are likely relevant for many regions of the Earth.

Consideration of laterally heterogeneous anisotropic structures has been intentionally neglected in this study, whose main purposes are to establish AxiSEM3D as a tool for modeling seismic

waveforms in arbitrary anisotropic global Earth models and to interrogate the behavior of relatively simple anisotropy scenarios. However, more realistic models that include lateral heterogeneity are needed to more fully explore the origin of $SKS - SKKS$ splitting discrepancies and the possible contributions of lowermost mantle anisotropy to $SK(K)S$ phases in the real Earth. This is particularly true given that in the lowermost mantle, the length scale of anisotropic heterogeneity may be smaller than the Fresnel zone of $SK(K)S$ phases; in practice, therefore, it is not clear how large the contribution to $SK(K)S$ splitting may be for realistic models of lowermost mantle anisotropy. Now that AxiSEM3D has been established as a computationally efficient tool for modeling wave propagation in an anisotropic Earth, work to understand the full-wave sensitivity of $SK(K)S$ phases to anisotropy in more realistic, heterogeneous Earth models is ongoing. In the case of 1D anisotropic models, such as those considered in this study, the Fourier spectral order required for a correct approximate solution to the 3D wave equation is dependent on the complexities of the underlying seismic velocity model. For a fully 3D anisotropic model, it is crucial to ensure that the Fourier spectral order of expansion is large enough to correctly account for the geometrical properties of the anisotropic model. As the cost of 3D anisotropic wavefield simulations increase with growing Fourier order, careful attention must be paid to the geographic dimensions of anisotropic domains in 3D models in order to preserve the computational advantages of the method with respect to 3D discrete spectral element methods.

7.4 Implications for the interpretation of $SKS - SKKS$ splitting discrepancies

Observations of discrepant $SKS - SKKS$ splitting for pairs of phases from the same event-station pair have been puzzling to shear wave splitting analysts since they were first documented by James & Assumpção (1996). A global study by Niu & Perez (2004) found that 95% of $SKS - SKKS$ observations globally were non-discrepant; that is, the SKS and $SKKS$ phases showed similar splitting behavior. In the remaining 5% of cases, however, the pairs exhibited discrepant splitting. Niu & Perez (2004) argued that because SKS and $SKKS$ phases have nearly identical ray paths in the upper mantle but diverge significantly in the lower mantle, discrepancies in $SKS-SKKS$ splitting should be attributed to anisotropy in the lower mantle. Restivo & Helffrich (2006)

suggested that anisotropy in the D'' layer is the most likely explanation for such discrepancies, and argued that topography on structures at or near the CMB may generate polarization anomalies, and thus splitting anomalies. A key aspect of the argument made by Restivo & Helffrich (2006) is that lateral gradients in structure at the base of the mantle are responsible for $SKS - SKKS$ splitting discrepancies. This notion was invoked by subsequent studies of $SKS-SKKS$ splitting discrepancies and lowermost mantle structure (e.g., Wang & Wen, 2007; Long, 2009), who argued that $SKS - SKKS$ splitting discrepancies should be interpreted in terms of a lateral gradient in seismic anisotropy at the base of the mantle (that is, with the SKS and $SKKS$ phases sampling a different geometry and/or strength of lowermost mantle anisotropy). More recent papers that have been informed by forward modeling studies (e.g., Ford et al., 2015; Creasy et al., 2019) have explicitly acknowledged the possibility that $SKS-SKKS$ splitting discrepancies can arise from homogenous anisotropy at the base of the mantle (e.g., Long & Lynner, 2015; Deng et al., 2017; Wolf et al., 2019; Reiss et al., 2019). In this case, the anisotropy must be present in a geometry that splits SKS and $SKKS$ phases differently.

While many authors have interpreted $SKS - SKKS$ splitting discrepancies as reflecting a contribution from anisotropy in the lower(most) mantle, other workers have questioned the extent to which anisotropy in the upper mantle may give rise to such discrepancies (or to discrepancies in splitting between SKS phases measured at the same station at similar backazimuths and incidence angles). For example, Monteiller & Chevrot (2010) documented differences in transverse component waveforms for pairs of SKS and $SKKS$ phases from nearby earthquakes, and pointed out that the variability between phases coming from nearby directions is of similar magnitude to the variability documented in previous studies of$SKS - SKKS$ splitting discrepancies that invoked D'' anisotropy as an explanation. Monteiller & Chevrot (2010) suggested that noise on the transverse component waveforms was the most likely explanation for these discrepancies, although other workers have argued that strong discrepancies measured on seismograms with relatively low noise levels cannot be due (solely) to noise (Long, 2009; Lynner & Long, 2014; Long & Lynner, 2015). In a later paper, Monteiller & Chevrot (2011) documented differences in estimated SKS splitting parameters for stations in southern California between their measurements, obtained with

the splitting intensity method, and previously published measurements; again, they attributed these discrepancies to the presence of noise and to differences in processing and measurement methods. Finally, Lin et al. (2014a) showed that full-wave effects can cause splitting discrepancies between SKS and $SKKS$ phases for the same event-station pairs of up to $\sim 0.3s$ at certain azimuths for models that only include homogeneous upper mantle anisotropy, as discussed in section 4.

What insights do our simulations give us into the interpretations of $SKS - SKKS$ splitting discrepancies? Our documentation of predicted $SKS - SKKS$ splitting discrepancies for both upper and lowermost mantle anisotropy models demonstrates that such discrepancies can arise from a physical cause, although of course the effects of noise must be considered for actual data. Similar to Lin et al. (2014a), we found that modest splitting intensity discrepancies (typically up to $0.2s$, with a few values up to $0.4s$) can arise from homogeneous upper mantle anisotropy models, possibly influenced by the interference of other phases in the $SK(K)S$ time window. Our simulations showed that much larger $SKS - SKKS$ splitting intensity discrepancies can arise from lowermost mantle anisotropy models (up to $\sim 1.0s$ or greater for post-perovskite; see Figure 13). Therefore, our work shows that both upper and lowermost mantle anisotropy may potentially contribute to $SKS-SKKS$ splitting intensity discrepancies for simple, homogeneous anisotropic models. Ongoing work that extends to models that include realistic 3D heterogeneity in anisotropic structure will answer the question of whether our general finding that lowermost mantle anisotropy models predict substantially stronger $SKS-SKKS$ splitting discrepancies than upper mantle models holds for more complex models. Particularly because $SK(K)S$ phases have large zones of sensitivity at the base of the mantle (e.g., Zhao & Chevrot, 2011), and because there may be heterogeneity in lowermost mantle anisotropy on length scales shorter than the Fresnel zones of the $SK(K)S$ waves under study, lowermost mantle anisotropy may contribute less to the splitting of $SK(K)S$ phases in practice than the results from laterally homogeneous models suggest. Furthermore, for actual, noisy data that reflects complex Earth structure, the effects of noise, phase interference, and complex wave propagation effects on apparent splitting parameters must be carefully considered.

Our lowermost mantle simulations also reinforce the notion that discrepant splitting behavior

between SKS and $SKKS$ phases can arise even in models that feature laterally homogeneous anisotropic structure in the lowermost mantle. While $SKS - SKKS$ splitting discrepancies are often taken to imply a lateral gradient in anisotropy between the respective D'' pierce points of the SKS and $SKKS$ phases (e.g., Long, 2009), our simulations (and previous work by others, including work based on ray theoretical approximations) show that homogeneous anisotropy can give rise to such discrepancies. $SKS - SKKS$ splitting discrepancies, when interpreted in the context of lowermost mantle anisotropy, should therefore be taken to imply a contribution to splitting from anisotropy sampled by one or both phases (e.g., Lynner & Long, 2014; Long & Lynner, 2015; Deng et al., 2017; Reiss et al., 2019), rather than to require a lateral gradient in D'' anisotropy.

8 CONCLUSION

We have presented a new wavefield modeling strategy to introduce the effects of general anisotropy in global models using the pseudo-spectral element code AxiSEM3D. The implementation of arbitrary anisotropy is accomplished by describing the elastic properties of the seismic domain in terms of the full elastic tensor with 21 independent coefficients. We have carried out global wavefield simulations for models that include anisotropy in the upper and lowermost mantle, reaching frequencies as high as $0.2Hz$ with relatively modest computational resources. We benchmarked our implementation against known reference solutions for simple upper mantle models, and then investigated the behavior of $SK(K)S$ phases for models that include upper mantle anisotropy (in HTI and orthorhombic geometries) as well as those that include anisotropy at the base of the mantle (for possible bridgmanite and post-perovskite CPO scenarios). We carried out shear wave splitting analysis (both the traditional transverse component minimization method and the splitting intensity method) on synthetic waveforms for the suite of global anisotropic models. These tests revealed that shear wave splitting, as manifested in the full-wavefield simulations, behaves similarly to the predictions of ray theory to first order, but some departures from ray theoretical behavior (due to full waveform effects) are found. Our results indicate that although some $SKS - SKKS$ splitting intensity discrepancies arise from anisotropic upper mantle models, par-

ticularly when low symmetry classes (e.g. orthorhombic) are considered, these are of modest amplitude (generally less than $0.2s$, with a few discrepancies up to $0.4s$). On the other hand, we find that realistic lowermost mantle anisotropy scenarios can cause significant splitting (up to $\sim 1s$) of $SK(K)S$ waveforms when full wave propagation is taken into account, with $SKS - SKKS$ splitting intensity discrepancies up to $\sim 1s$ or greater. The cross-validation test with the discrete spectral element solver SPECFEM3D_GLOBE further highlights the capability of AxiSEM3D to handle increasingly complex Earth models, including those with arbitrary anisotropic symmetry, without loss of accuracy and with accessible computing resources. In the future, AxiSEM3D will be used to investigate the behavior of $SK(K)S$ phases in the presence of lateral heterogeneity in anisotropic structure, paving the way for more realistic consideration of full wavefield effects when interpreting shear wave splitting measurements, particularly due to D'' anisotropy.

9 ACKNOWLEDGEMENT

We are grateful to Neala Creasy and Miriam Reiss for fruitful discussions and assistance with shear wave splitting measurements. We thank Vadim Levin and the Rutgers University seismology group for insightful discussions that helped lead us to our modeling strategy. We thank Andy Nowacki for sharing his code and providing detailed instructions to help us understand the implementation of full anisotropy in SPECFEM3D_GLOBE. We thank the Yale Center for Research Computing for guidance and use of the research computing infrastructure, specifically the Grace cluster. We also acknowledge use of the U.K. supercomputer ARCHER. We are also grateful to the editor, Professor Li Zhao, and another reviewer for their constructive comments that helped us improve our manuscript. This work was funded by the U.S. National Science Foundation via grant EAR-1547499 to MDL. KL and TNM acknowledge support by NERC Grant NE/R012199/1. For the collaboration of this work, KL worked as a postdoctoral associate at Yale University, funded via NSF grant EAR-1610612 to Jun Korenaga.

References

Abramson, E. H., Brown, J. M., Slutsky, L. J., & Zaug, J., 1997. The elastic constants of San Carlos olivine to 17 GPa, *Journal of Geophysical Research: Solid Earth*, **102**(B6), 12253–12263.

Anderson, D., 1989. *Theory of the Earth*, Blackwell Science.

Anderson, D. L., 1961. Elastic wave propagation in layered anisotropic media, *Journal of Geophysical Research*, **66**(9), 2953–2963.

Anderson, D. L. & Dziewonski, A. M., 1982. Upper mantle anisotropy: evidence from free oscillations, *Geophysical Journal International*, **69**(2), 383–404.

Auer, L., Boschi, L., Becker, T. W., Nissen-Meyer, T., & Giardini, D., 2014. Savani: A variable resolution whole-mantle model of anisotropic shear velocity variations based on multiple data sets, *Journal of Geophysical Research: Solid Earth*, **119**(4), 3006–3034.

Babuska, V. & Cara, M., 1991. *Seismic Anisotropy in the Earth*, Springer Netherlands, 1st edn.

Barruol, G. & Kern, H., 1996. Seismic anisotropy and shear-wave splitting in lower-crustal and upper-mantle rocks from the Ivrea Zone—experimental and calculated data, *Physics of the Earth and Planetary Interiors*, **95**(3-4), 175–194.

Becker, T. W., Chevrot, S., Schulte-Pelkum, V., & Blackman, D. K., 2006. Statistical properties of seismic anisotropy predicted by upper mantle geodynamic models, *Journal of Geophysical Research*, **111**(B8).

Beghein, C. & Trampert, J., 2003. Robust normal mode constraints on inner-core anisotropy from model space search, *Science*, **299**(5606), 552–555.

Beghein, C., Resovsky, J., & van der Hilst, R. D., 2008. The signal of mantle anisotropy in the coupling of normal modes, *Geophysical Journal International*, **175**(3), 1209–1234.

Ben Ismaïl, W. & Mainprice, D., 1998. An olivine fabric database: an overview of upper mantle fabrics and seismic anisotropy, *Tectonophysics*, **296**(1-2), 145–157.

Browaeys, J. T. & Chevrot, S., 2004. Decomposition of the elastic tensor and geophysical applications, *Geophysical Journal International*, **159**(2), 667–678.

Buehler, J. S. & Shearer, P. M., 2017. Uppermost mantle seismic velocity structure beneath USArray, *Journal of Geophysical Research: Solid Earth*, **122**(1), 436–448.

Chevrot, S., 2000. Multichannel analysis of shear wave splitting, *Journal of Geophysical Research: Solid Earth*, **105**(B9), 21579–21590.

Chevrot, S., 2006. Finite-frequency vectorial tomography: a new method for high-resolution imaging of upper mantle anisotropy, *Geophysical Journal International*, **165**(2), 641–657.

Cottaar, S. & Romanowicz, B., 2013. Observations of changing anisotropy across the southern margin of the African LLSVP, *Geophysical Journal International*, **195**(2), 1184–1195.

Cottaar, S., Li, M., McNamara, A. K., Romanowicz, B., & Wenk, H.-R., 2014. Synthetic seismic anisotropy models within a slab impinging on the coremantle boundary, *Geophysical Journal International*, **199**(1), 164–177.

Creasy, N., Long, M. D., & Ford, H. A., 2017. Deformation in the lowermost mantle beneath Australia from observations and models of seismic anisotropy, *Journal of Geophysical Research: Solid Earth*.

Creasy, N., Pisconti, A., Long, M. D., Thomas, C., & Wookey, J., 2019. Constraining lowermost mantle anisotropy with body waves: a synthetic modelling study, *Geophysical Journal International*, **217**(2), 766–783.

Crotwell, H. P., Owens, T. J., & Ritsema, J., 1999. The TauP toolkit: Flexible seismic travel-time and ray-path utilities, *Seismological Research Letters*, **70**, 154 – 160.

Deng, J., Long, M. D., Creasy, N., Wagner, L., Beck, S., Zandt, G., Tavera, H., & Minaya, E., 2017. Lowermost mantle anisotropy near the eastern edge of the Pacific LLSVP: constraints from SKS-SKKS splitting intensity measurements, *Geophysical Journal International*, **210**(2), 774–786.

Dziewonski, A. M. & Anderson, D. L., 1981. Preliminary reference Earth model, *Physics of the Earth and Planetary Interiors*, **25**(4), 297–356.

Eakin, C. M. & Long, M. D., 2013. Complex anisotropy beneath the peruvian flat slab from frequency-dependent, multiple-phase shear wave splitting analysis, *Journal of Geophysical Research: Solid Earth*, **118**(9), 4794–4813.

Favier, N. & Chevrot, S., 2003. Sensitivity kernels for shear wave splitting in transverse isotropic media, *Geophysical Journal International*, **153**(1), 213–228.

Favier, N., Chevrot, S., & Komatitsch, D., 2004. Near-field influence on shear wave splitting and traveltime sensitivity kernels, *Geophysical Journal International*, **156**(3), 467–482.

Ferreira, A. M. G., Faccenda, M., Sturgeon, W., Chang, S.-J., & Schardong, L., 2019. Ubiquitous lower-mantle anisotropy beneath subduction zones, *Nature Geoscience*, **12**(4), 301–306.

Foley, B. J. & Long, M. D., 2011. Upper and mid-mantle anisotropy beneath the Tonga slab, *Geophysical Research Letters*, **38**(2), n/a–n/a.

Ford, H. A. & Long, M. D., 2015. A regional test of global models for flow, rheology, and seismic anisotropy at the base of the mantle, *Physics of the Earth and Planetary Interiors*, **245**, 71–75.

Ford, H. A., Long, M. D., He, X., & Lynner, C., 2015. Lowermost mantle flow at the eastern edge of the African Large Low Shear Velocity Province, *Earth and Planetary Science Letters*, **420**, 12–22.

Forsyth, D. W., 1975. The early structural evolution and anisotropy of the oceanic upper mantle, *Geophysical Journal International*, **43**(1), 103–162.

Grund, M. & Ritter, J. R. R., 2018. Widespread seismic anisotropy in Earth's lowermost mantle beneath the Atlantic and Siberia, *Geology*, **47**(2), 123–126.

He, X. & Long, M. D., 2011. Lowermost mantle anisotropy beneath the northwestern Pacific: Evidence from PcS, ScS, SKS, and SKKS phases, *Geochemistry, Geophysics, Geosystems*, **12**(12), n/a–n/a.

Hernlund, J. W., Thomas, C., & Tackley, P. J., 2005. A doubling of the post-perovskite phase boundary and structure of the earth's lowermost mantle, *Nature*, **434**(7035), 882–886.

Hess, H. H., 1964. Seismic anisotropy of the uppermost mantle under oceans, *Nature*, **203**(4945), 629–631.

Houser, C., 2007. Constraints on the presence or absence of post-perovskite in the lowermost mantle from long-period seismology, in *Geophysical Monograph Series*, pp. 191–216, American Geophysical Union.

Isaak, D. G., 1992. High-temperature elasticity of iron-bearing olivines, *Journal of Geophysical Research: Solid Earth*, **97**(B2), 1871–1885.

Jaeken, J. W. & Cottenier, S., 2016. Solving the Christoffel equation: Phase and group velocities,

Computer Physics Communications, **207**, 445–451.

James, D. E. & Assumpção, M., 1996. Tectonic implications of S-wave anisotropy beneath SE Brazil, *Geophysical Journal International*, **126**(1), 1–10.

Karato, S., Jung, H., Katayama, I., & Skemer, P., 2008. Geodynamic significance of seismic anisotropy of the upper mantle: New insights from laboratory studies, *Annual Review of Earth and Planetary Sciences*, **36**(1), 59–95.

Koelemeijer, P., Schuberth, B. S. A., Davies, D. R., Deuss, A., & Ritsema, J., 2018. Constraints on the presence of post-perovskite in Earth's lowermost mantle from tomographic-geodynamic model comparisons, *Earth and Planetary Science Letters*, **494**, 226–238.

Komatitsch, D. & Tromp, J., 2002a. Spectral-element simulations of global seismic wave propagation — I. Validation, *Geophysical Journal International*, **149**(2), 390–412.

Komatitsch, D. & Tromp, J., 2002b. Spectral-element simulations of global seismic wave propagation — II. Three-dimensional models, oceans, rotation and self-gravitation, *Geophysical Journal International*, **150**(1), 303–318.

Leng, K., Nissen-Meyer, T., & van Driel, M., 2016. Efficient global wave propagation adapted to 3-D structural complexity: a pseudospectral/spectral-element approach, *Geophysical Journal International*, **207**(3), 1700–1721.

Leng, K., Nissen-Meyer, T., van Driel, M., Hosseini, K., & Al-Attar, D., 2019. AxiSEM3D: broad-band seismic wavefields in 3-D global earth models with undulating discontinuities, *Geophysical Journal International*, **217**(3), 2125–2146.

Levin, V. & Park, J., 1998. P-SH conversions in layered media with hexagonally symmetric anisotropy: A CookBook, *Pure and Applied Geophysics*, **151**(2-4), 669–697.

Levin, V., Menke, W., & Park, J., 1999. Shear wave splitting in the Appalachians and the Urals: A case for multilayered anisotropy, *Journal of Geophysical Research: Solid Earth*, **104**(B8), 17975–17993.

Lin, Y.-P., Zhao, L., & Hung, S.-H., 2014a. Full-wave effects on shear wave splitting, *Geophysical Research Letters*, **41**(3), 799–804.

Lin, Y.-P., Zhao, L., & Hung, S.-H., 2014b. Full-wave multiscale anisotropy tomography in

Southern California, *Geophysical Research Letters*, **41**(24), 8809–8817.

Long, M. D., 2009. Complex anisotropy in D″ beneath the Eastern Pacific from SKS–SKKS splitting discrepancies, *Earth and Planetary Science Letters*, **283**(1-4), 181–189.

Long, M. D., 2013. CONSTRAINTS ON SUBDUCTION GEODYNAMICS FROM SEISMIC ANISOTROPY, *Reviews of Geophysics*, **51**(1), 76–112.

Long, M. D. & Becker, T. W., 2010. Mantle dynamics and seismic anisotropy, *Earth and Planetary Science Letters*, **297**, 341–354.

Long, M. D. & Lynner, C., 2015. Seismic anisotropy in the lowermost mantle near the Perm Anomaly, *Geophysical Research Letters*, **42**(17), 7073–7080.

Long, M. D. & Silver, P. G., 2009. Shear wave splitting and mantle anisotropy: Measurements, interpretations, and new directions, *Surveys in Geophysics*, **30**(4-5), 407–461.

Long, M. D. & van der Hilst, R. D., 2005. Estimating shear-wave splitting parameters from broadband recordings in Japan: A comparison of three methods, *Bulletin of the Seismological Society of America*, **95**(4), 1346–1358.

Long, M. D., de Hoop, M. V., & van der Hilst, R. D., 2008. Wave-equation shear wave splitting tomography, *Geophysical Journal International*, **172**(1), 311–330.

Lynner, C. & Long, M. D., 2014. Lowermost mantle anisotropy and deformation along the boundary of the African LLSVP, *Geophysical Research Letters*, **41**(10), 3447–3454.

Lynner, C. & Long, M. D., 2015. Heterogeneous seismic anisotropy in the transition zone and uppermost lower mantle: evidence from South America, Izu-Bonin and Japan, *Geophysical Journal International*, **201**(3), 1545–1552.

Malvern, L. E., 1969. *Introduction to the Mechanics of a Continuous Medium*, Pearson.

Mao, Z., Fan, D., Lin, J.-F., Yang, J., Tkachev, S. N., Zhuravlev, K., & Prakapenka, V. B., 2015. Elasticity of single-crystal olivine at high pressures and temperatures, *Earth and Planetary Science Letters*, **426**, 204–215.

Marson-Pidgeon, K. & Savage, M. K., 2004. Modelling shear wave splitting observations from Wellington, New Zealand, *Geophysical Journal International*, **157**(2), 853–864.

Mondal, P. & Long, M. D., 2019. A model space search approach to finite-frequency SKS split-

ting intensity tomography in a reduced parameter space, *Geophysical Journal International*, **217**(1), 238–256.

Montagner, J. P., 2002. Upper mantle low anisotropy channels below the Pacific Plate, *Earth and Planetary Science Letters*, **202**(2), 263–274.

Monteiller, V. & Chevrot, S., 2010. How to make robust splitting measurements for single-station analysis and three-dimensional imaging of seismic anisotropy, *Geophysical Journal International*, pp. no–no.

Monteiller, V. & Chevrot, S., 2011. High-resolution imaging of the deep anisotropic structure of the San Andreas fault system beneath Southern California, *Geophysical Journal International*, **186**(2), 418–446.

Moulik, P. & Ekström, G., 2014. An anisotropic shear velocity model of the Earth's mantle using normal modes, body waves, surface waves and long-period waveforms, *Geophysical Journal International*, **199**(3), 1713–1738.

Murakami, M., Hirose, K., Kawamura, K., Sata, N., & Ohishi, Y., 2004. Post-perovskite phase transition in $MgSiO_3$, *Science*, **304**(5672), 855–858.

Nissen-Meyer, T., van Driel, M., Sthler, S. C., Hosseini, K., Hempel, S., Auer, L., Colombi, A., & Fournier, A., 2014. AxiSEM: broadband 3-D seismic wavefields in axisymmetric media, *Solid Earth*, **5**(1), 425–445.

Niu, F. & Perez, A. M., 2004. Seismic anisotropy in the lower mantle: A comparison of waveform splitting of SKS and SKKS, *Geophysical Research Letters*, **31**(24).

Nowacki, A. & Wookey, J., 2016. The limits of ray theory when measuring shear wave splitting in the lowermost mantle withScS waves, *Geophysical Journal International*, **207**(3), 1573–1583.

Nowacki, A., Wookey, J., & Kendall, J.-M., 2010. Deformation of the lowermost mantle from seismic anisotropy, *Nature*, **467**(7319), 1091–1094.

Nowacki, A., Wookey, J., & Kendall, J.-M., 2011. New advances in using seismic anisotropy, mineral physics and geodynamics to understand deformation in the lowermost mantle, *Journal of Geodynamics*, **52**(3-4), 205–228.

Park, J. & Yu, Y., 1993. Seismic determination of elastic anisotropy and mantle flow, *Science*,

261(5125), 1159–1162.

Peter, D., Komatitsch, D., Luo, Y., Martin, R., Le Goff, N., Casarotti, E., Le Loher, P., Magnoni, F., Liu, Q., Blitz, C., Nissen-Meyer, T., Basini, P., & Tromp, J., 2011. Forward and adjoint simulations of seismic wave propagation on fully unstructured hexahedral meshes, *Geophysical Journal International*, **186**(2), 721–739.

Rao, B. P., Kumar, M. R., & Singh, A., 2017. Anisotropy in the lowermost mantle beneath the Indian Ocean Geoid Low from ScS splitting measurements, *Geochemistry, Geophysics, Geosystems*, **18**(2), 558–570.

Reiss, M., Long, M., & Creasy, N., 2019. Lowermost mantle anisotropy beneath africa from differential SKS-SKKS shear-wave splitting, *Journal of Geophysical Research: Solid Earth*.

Reiss, M. C. & Rümpker, G., 2017. SplitRacer: MATLAB code and GUI for semiautomated analysis and interpretation of teleseismic shear-wave splitting, *Seismological Research Letters*, **88**(2A), 392–409.

Restivo, A. & Helffrich, G., 2006. Core-mantle boundary structure investigated SKS and SKKS polarization anomalies, *Geophysical Journal International*, **165**(1), 288–302.

Ritsema, J., Deuss, A., van Heijst, J., & J.H., W., 2011. S40RTS: a degree-40 shear-velocity model for the mantle from new Rayleigh wave dispersion, teleseismic traveltime and normal-mode splitting function measurements, *Geophysical Journal International*, **184**(3), 1223–1236.

Roy, S. K., M., R. K., & D., S., 2014. Upper and lower mantle anisotropy inferred from comprehensive SKS and SKKS splitting measurements from India, *Earth and Planetary Science Letters*, **392**, 192–206.

Savage, M. K., 1999. Seismic anisotropy and mantle deformation: What have we learned from shear wave splitting?, *Reviews of Geophysics*, **37**(1), 65–106.

Schaeffer, A. J., Lebedev, S., & Becker, T. W., 2016. Azimuthal seismic anisotropy in the Earth's upper mantle and the thickness of tectonic plates, *Geophysical Journal International*, **207**(2), 901–933.

Schulte-Pelkum, V., Masters, G., & Shearer, P. M., 2001. Upper mantle anisotropy from long-period P polarization, *Journal of Geophysical Research: Solid Earth*, **106**(B10), 21917–21934.

Servali, A., Long, M. D., Park, J., Benoit, M. H., & Aragon, J. C., 2020. Love-to-Rayleigh scattering across the eastern North American passive margin, *Tectonophysics*, **776**, 228321.

Sieminski, A., Paulssen, H., Trampert, J., & Tromp, J., 2008. Finite-frequency SKS splitting: Measurement and sensitivity kernels, *Bulletin of the Seismological Society of America*, **98**(4), 1797–1810.

Silver, P. G., 1996. Seismic anisotropy beneath the continents: Probing the depths of geology, *Annual Review of Earth and Planetary Sciences*, **24**, 385–432.

Silver, P. G. & Chan, W. W., 1988. Implications for continental structure and evolution from seismic anisotropy, *Nature*, **335**(6185), 34–39.

Silver, P. G. & Chan, W. W., 1991. Shear wave splitting and subcontinental mantle deformation, *Journal of Geophysical Research: Solid Earth*, **96**(B10), 16429–16454.

Silver, P. G. & Savage, M. K., 1994. The interpretation of shear-wave splitting parameters in the presence of two anisotropic layers, *Geophysical Journal International*, **119**(3), 949–963.

Skemer, P. & Hansen, L. N., 2016. Inferring upper-mantle flow from seismic anisotropy: An experimental perspective, *Tectonophysics*, **668-669**, 1–14.

Tesoniero, A., Auer, L., Boschi, L., & Cammarano, F., 2015. Hydration of marginal basins and compositional variations within the continental lithospheric mantle inferred from a new global model of shear and compressional velocity, *Journal of Geophysical Research: Solid Earth*, **120**(11), 7789–7813.

Tommasi, A., Goryaeva, A., Carrez, P., Cordier, P., & Mainprice, D., 2018. Deformation, crystal preferred orientations, and seismic anisotropy in the Earth's D'' layer, *Earth and Planetary Science Letters*, **492**, 35–46.

Tromp, J., 1995. Normal-mode splitting due to inner-core anisotropy, *Geophysical Journal International*, **121**(3), 963–968.

Vinnik, L. P., Farra, V., & Romanowicz, B., 1989. Azimuthal anisotropy in the earth from observations of SKS at GEOSCOPE and NARS broadband stations, *Bulletin of the Seismological Society of America*, **79**(5), 1542–1558.

Walker, A. M. & Wookey, J., 2012. MSAT —A new toolkit for the analysis of elastic and seismic

anisotropy, *Computers & Geosciences*, **49**, 81–90.

Walker, A. M., Forte, A. M., Wookey, J., Nowacki, A., & Kendall, J.-M., 2011. Elastic anisotropy of D'' predicted from global models of mantle flow, *Geochemistry, Geophysics, Geosystems*, **12**(10), n/a–n/a.

Walker, A. M., Dobson, D. P., Wookey, J., Nowacki, A., & Forte, A. M., 2018. The anisotropic signal of topotaxy during phase transitions in D'', *Physics of the Earth and Planetary Interiors*, **276**, 159–171.

Wang, Y. & Wen, L., 2007. Complex seismic anisotropy at the border of a very low velocity province at the base of the Earth's mantle, *Journal of Geophysical Research*, **112**(B9).

Wirth, E. A. & Long, M. D., 2014. A contrast in anisotropy across mid-lithospheric discontinuities beneath the central United State - a relic of craton formation, *Geology*, **42**(10), 851–854.

Wolf, J., Creasy, N., Pisconti, A., Long, M. D., & Thomas, C., 2019. An investigation of seismic anisotropy in the lowermost mantle beneath Iceland, *Geophysical Journal International*, **219**(Supplement_1), S152–S166.

Wolfe, C. J. & Silver, P. G., 1998. Seismic anisotropy of oceanic upper mantle: Shear wave splitting methodologies and observations, *Journal of Geophysical Research: Solid Earth*, **103**(B1), 749–771.

Wookey, J. & Kendall, J.-M., 2008. Constraints on lowermost mantle mineralogy and fabric beneath Siberia from seismic anisotropy, *Earth and Planetary Science Letters*, **275**(1-2), 32–42.

Wookey, J., Kendall, J.-M., & Rümpker, G., 2005a. Lowermost mantle anisotropy beneath the north Pacific from differential S-ScS splitting, *Geophysical Journal International*, **161**(3), 829–838.

Wookey, J., Stackhouse, S., Kendall, J.-M., Brodholt, J., & Price, G. D., 2005b. Efficacy of the post-perovskite phase as an explanation for lowermost-mantle seismic properties, *Nature*, **438**(7070), 1004–1007.

Yuan, K. & Beghein, C., 2013. Seismic anisotropy changes across upper mantle phase transitions, *Earth and Planetary Science Letters*, **374**, 132–144.

Zhao, L. & Chevrot, S., 2011. An efficient and flexible approach to the calculation of three-

dimensional full-wave Fréchet kernels for seismic tomography-II. numerical results, *Geophysical Journal International*, **185**(2), 939–954.

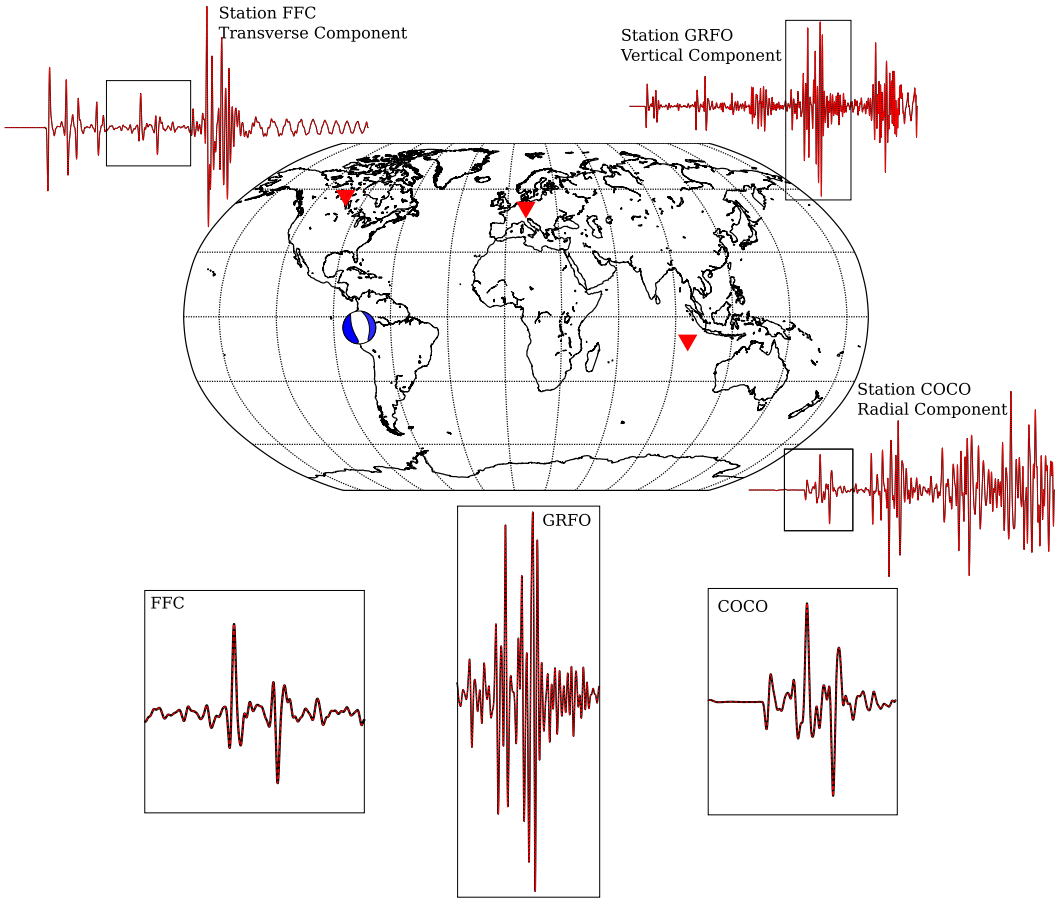

Figure 1. Map showing the source-receiver configuration settings and the synthetic results for the self-benchmarking tests computed using AxiSEM3D with the anisotropic PREM model (black seismograms) and the solution obtained using a description of the anisotropic PREM as C_{ijkl} (red seismograms). Three representative pairs of synthetic seismograms are plotted at three different locations. A close-up view of the synthetics is shown in the three boxes at the bottom of the figures for three different sections of the time series.

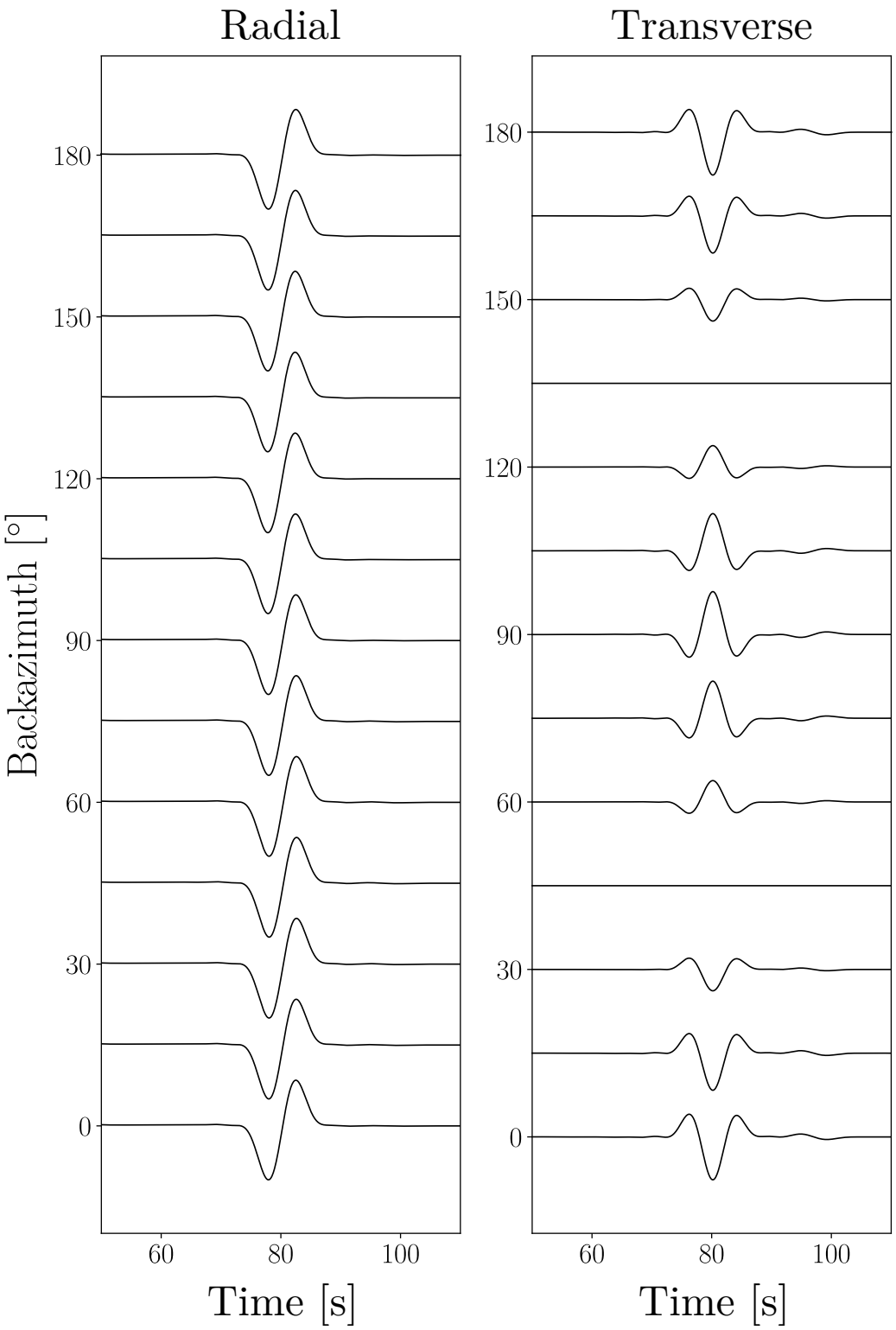

Figure 2. Synthetic seismograms computed for a vertically propagating shear wave in a $30km$ thick horizontally transverse isotropic (HTI) layer with 3% anisotropy. The amplitude of the transverse component is amplified by a factor of 10.

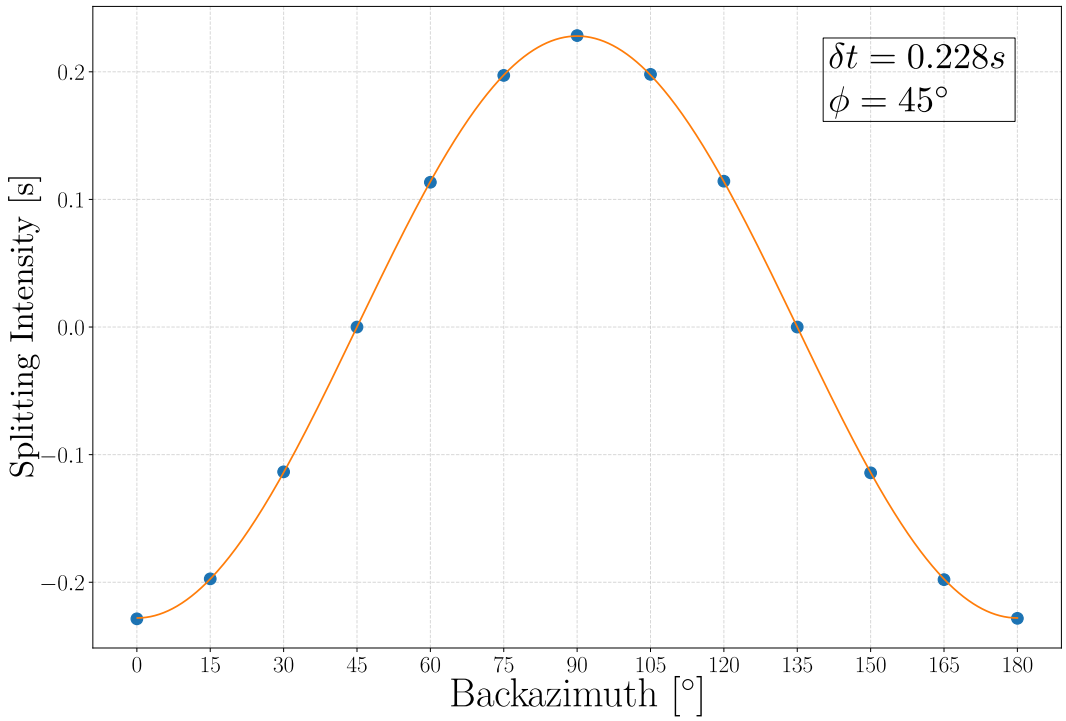

Figure 3. Result of the shear wave splitting intensity analysis performed on the synthetic seismograms of Fig. 2. The splitting intensity vector (blue dots) is computed following Chevrot (2000, eq. A4). The orange curve is the least square fit solution $s = \sin 2\theta(\phi - \phi_0)$, calculated over possible pairs of splitting intensity parameters ϕ and δt, that minimizes the misfit between the synthetic and the theoretical splitting intensity solution. The amplitude of the curve is $0.228s$ and its phase is $45°$.

Compare this figure with (Chevrot, 2000, Figure 3).

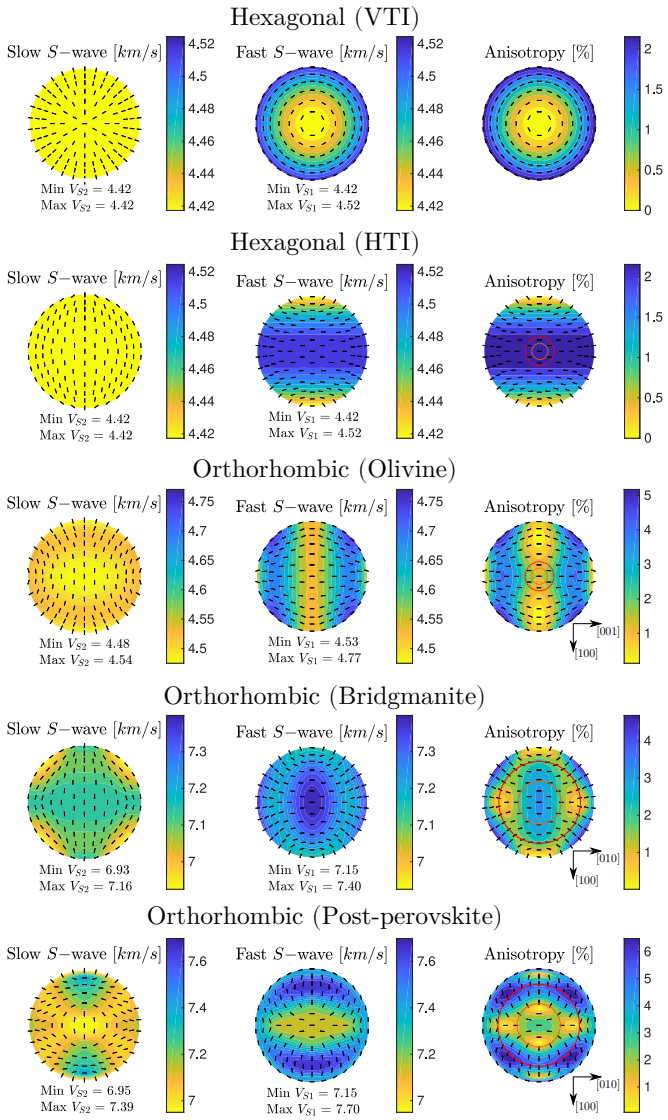

Figure 4. Polar view representation of different elasticity tensors belonging to different symmetry classes (from top to bottom hexagonal (VTI, HTI) and orthorhombic (olivine, bridgmanite, post-perovskite) used to describe the elastic and geometrical properties of the anisotropic regions tested in the different simulation settings. The magnitude of the slow and fast shear wave velocity and its polarization direction (black thick marks) are shown on the left and middle plots respectively. A measure of the anisotropy is shown on the right-hand side plot along with the fast shear wave polarization direction (black thick marks). The VTI, HTI, and olivine tensors are used in examples where the anisotropy is localized in the upper mantle whereas the bridgmanite and post-perovskite are used in the D''. The orientation of the othorombic crystals are specified by the 2 orthogonal crystallographic axes that lie in the horizontal plane. The dashed concentric circles in the HTI and olivine tensors mark the region of the piercing points for the SKS (orange) and $SKKS$ (red) phases in the upper mantle, while the solid circles indicate the region of the piercing points for the bridgmanite and post-perovskite crystals in the D'' layer.

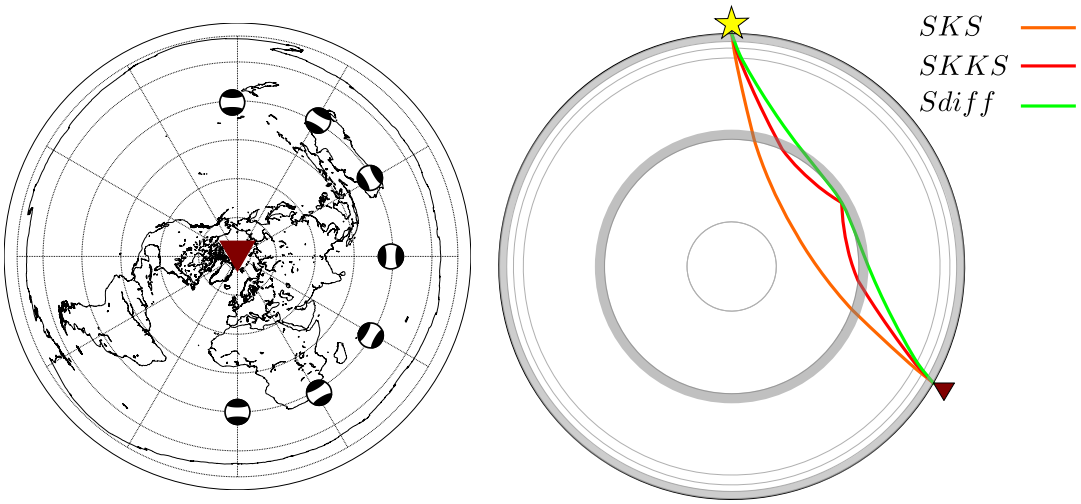

Figure 5. Left: Source-receiver distribution for global seismic wavefield simulations in anisotropic Earth-like models. The red triangle marks the center of the array of receivers located at the North Pole at a distance of $120°$ from the seismic sources. The sources span a fan of $180°$ along the azimuthal direction with inter-spacing of $15°$.

Right: Diagram of ray-theoretical paths of seismic S phases commonly used in share wave splitting analysis. The paths for SKS, $SKKS$ and S_{diff} are shown as reference for a source (star) and the receiver (red triangle) at $120°$ of epicentral distance. The shaded grey areas represent the two anisotropic regions between $24km$ and $220km$ in the upper mantle and $250km$ at the top of the Core Mantle Boundary in the D''. Paths are calculated using **TauP** (Crotwell et al., 1999) for the PREM velocity model (Dziewonski & Anderson, 1981)

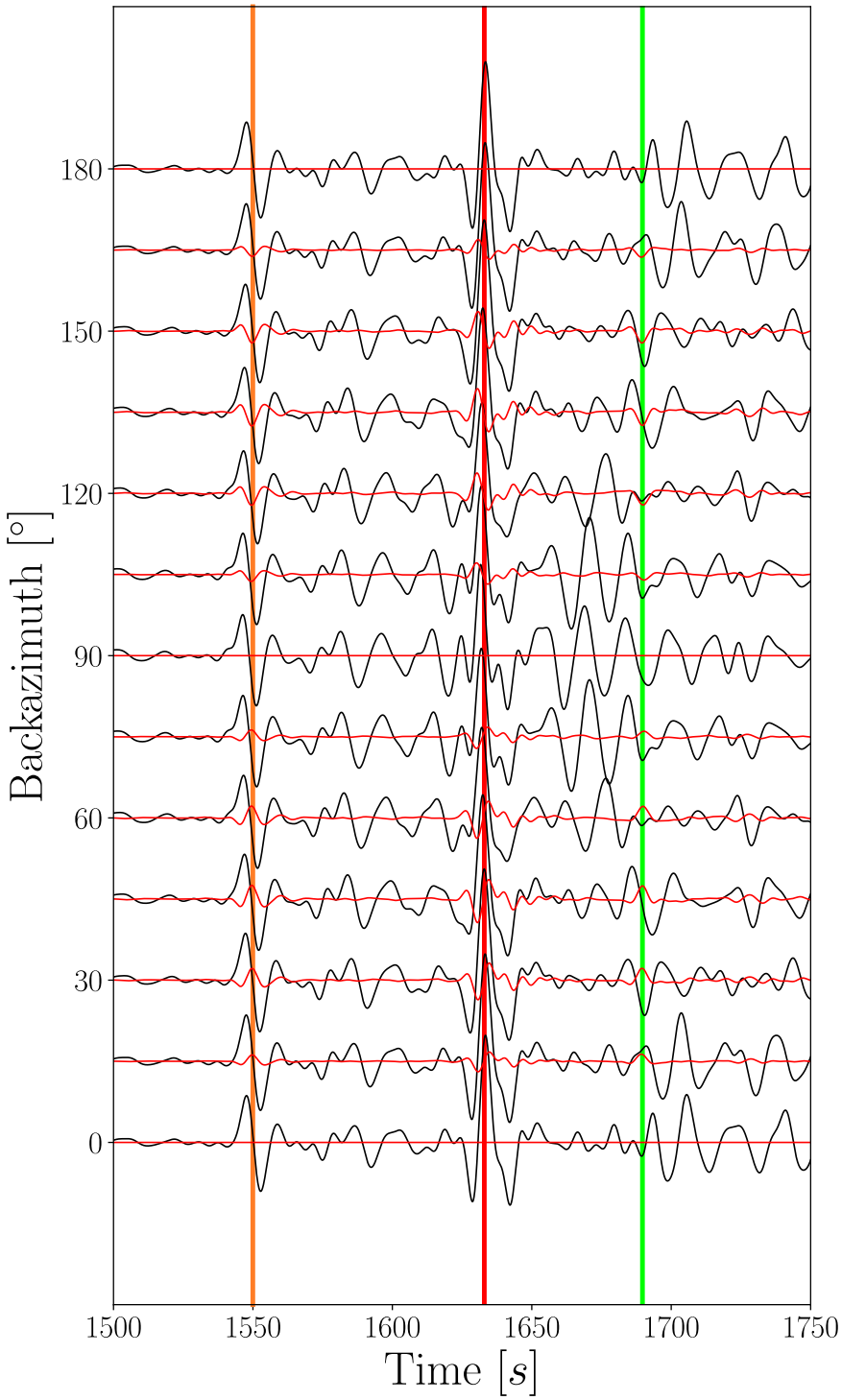

Figure 6. Synthetic seismograms computed for the PREM model with a HTI layer localized between 24 and $220km$ plotted against the backazimuth of the incoming seismic energy. The epicentral distance is 120°. The radial component is shown in black and the transverse is shown in red. Predicted arrival time for SKS, $SKKS$ and S_{diff} are shown as the vertical orange, red and green bars respectively.

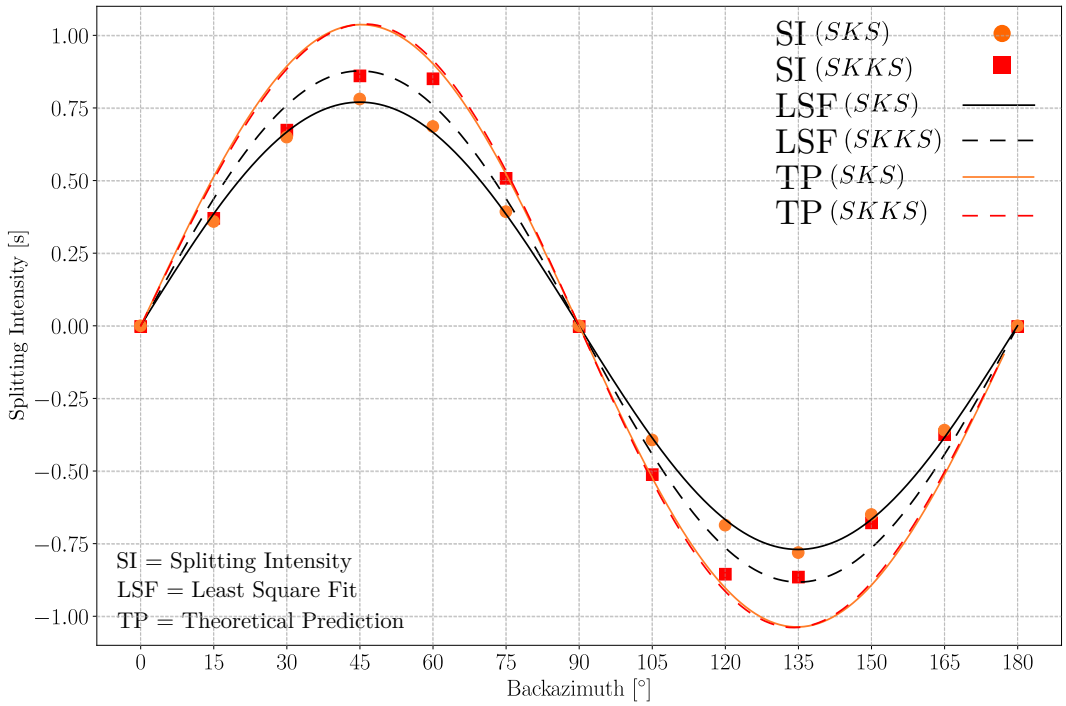

Figure 7. Shear wave splitting intensity analysis performed on the synthetic seismograms evaluated for the PREM model with HTI (see Figure 4, second row) localized between 24 and 220km depth. Values of the splitting intensity vector calculated for SKS are shown as orange circles while for $SKKS$ are shown as red squares. The black solid and dashed curves represent the two least square fit solutions for SKS and $SKKS$ respectively. The orange solid and dashed red lines are the ray-theoretical predicted splitting intensity vectors for SKS and $SKKS$ respectively, evaluated by solving the Christoffel equation for an elasticity tensor that was averaged over the depth range of a $\sim$ 200km thick anisotropic layer in the upper mantle.

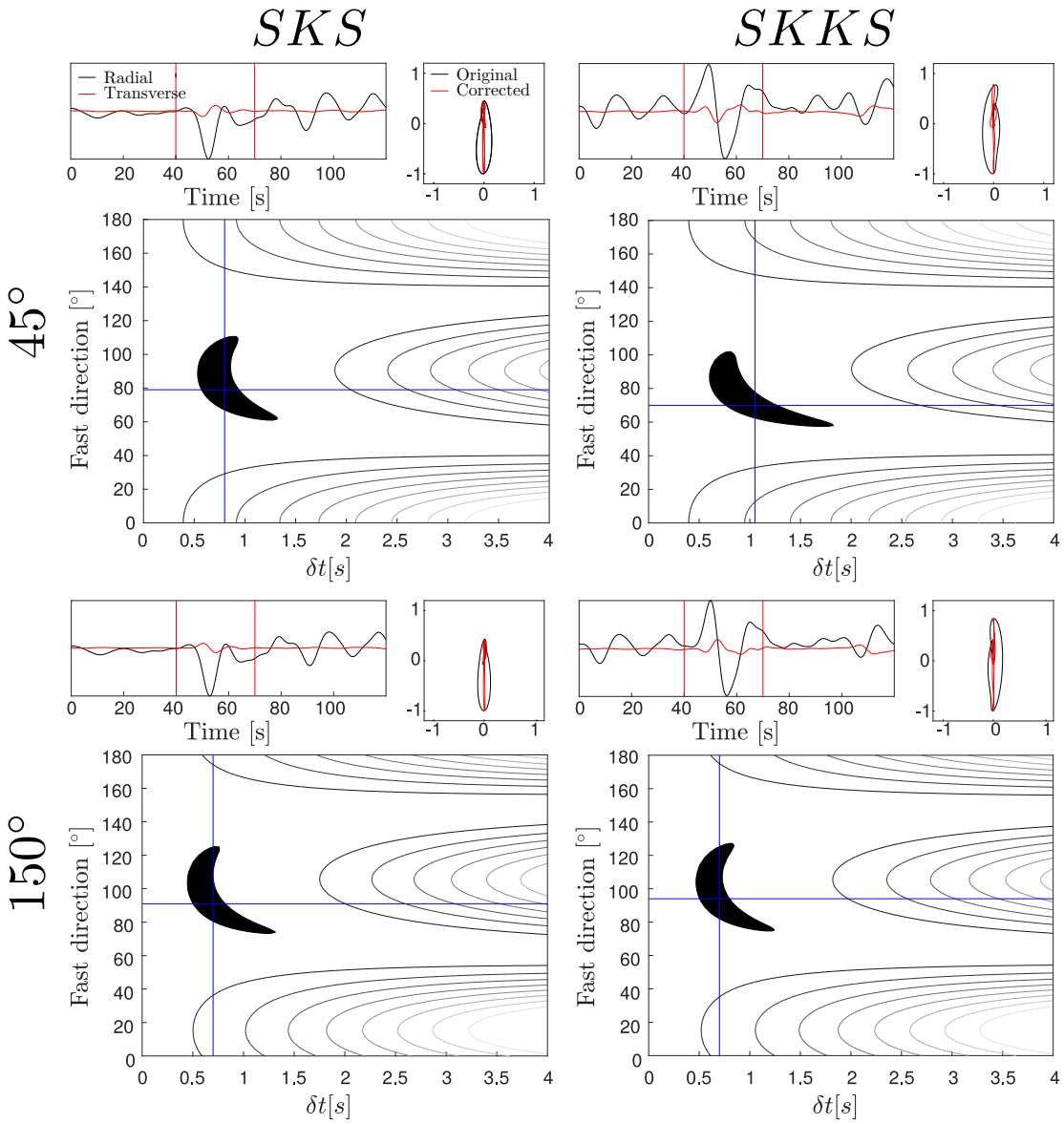

Figure 8. Shear wave splitting analysis performed using the transverse component minimization method (Silver & Chan, 1991) on the SKS (left) and $SKKS$ (right) phases for 2 representative backazimuthal propagation directions of the incoming seismic energy (45° and 150°). The synthetic seismograms are evaluated for a PREM model with a HTI layer localized between 24 and 220km as in Figure 7. Each panel is composed by 3 plots: On the top left a 120s long time-window with the radial (black) and transverse (red) component synthetic seismograms. The vertical red bars mark the phases on which the analysis is performed. On the top right corner we show the original and the corrected particle motion. In the bottom plot we show the energy map with the calculated splitting parameters and the 95% confidence interval as the shaded black area. For this configuration SKS and $SKKS$ yield a comparable results for both fast direction axis and delay-time.

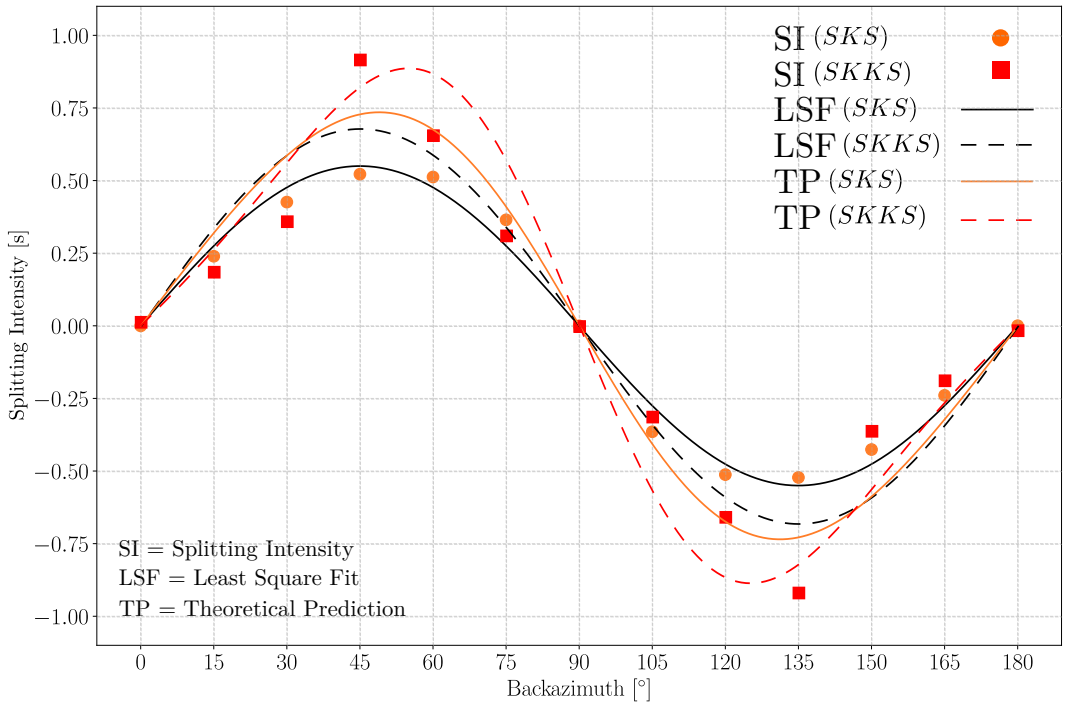

Figure 9. Same as Fig. 7 but with the anisotropic region in upper mantle between 24 and 220km described with an orthorhombic elasticity tensor (see Fig. 4, third row). The elastic properties of the tensor are the result of a linear mixture of 30% of San Carlos single crystal olivine from Abramson et al. (1997) and 70% PREM. The least square fit solutions and the theoretical predicted splitting intensity vectors are also plotted with the same color code used in Fig. 7.

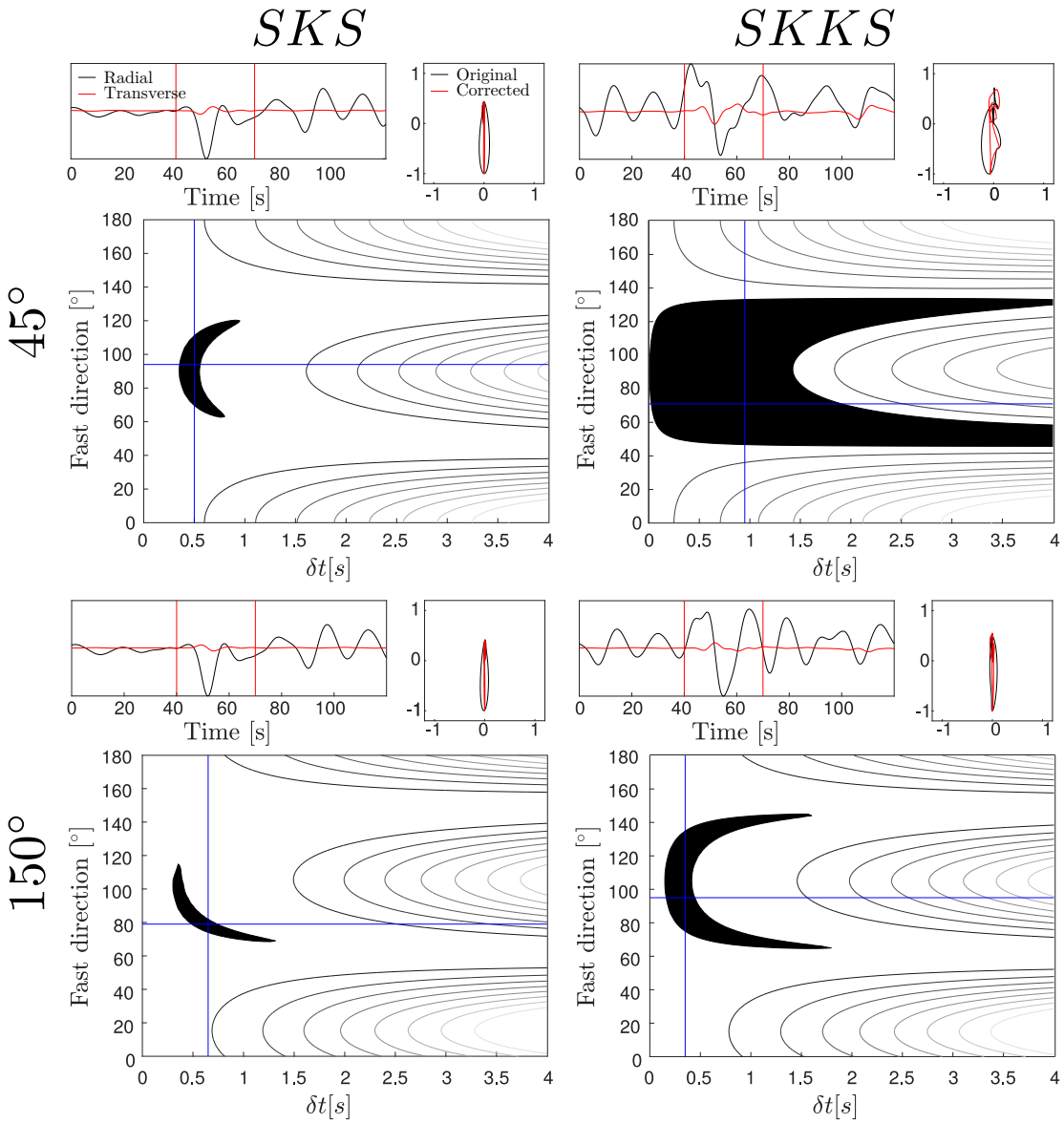

Figure 10. Same as Fig. 8 but with the anisotropic region in the upper mantle between 24 and 220km being descried with an elasticity tensor of orthorhombic class which mimics the elastic properties of a horizontally strained olivine (see Figure 4, third row). The splitting parameter estimates are less well constrained, with larger formal errors, than for the hexagonal upper mantle simulation shown in Fig. 8

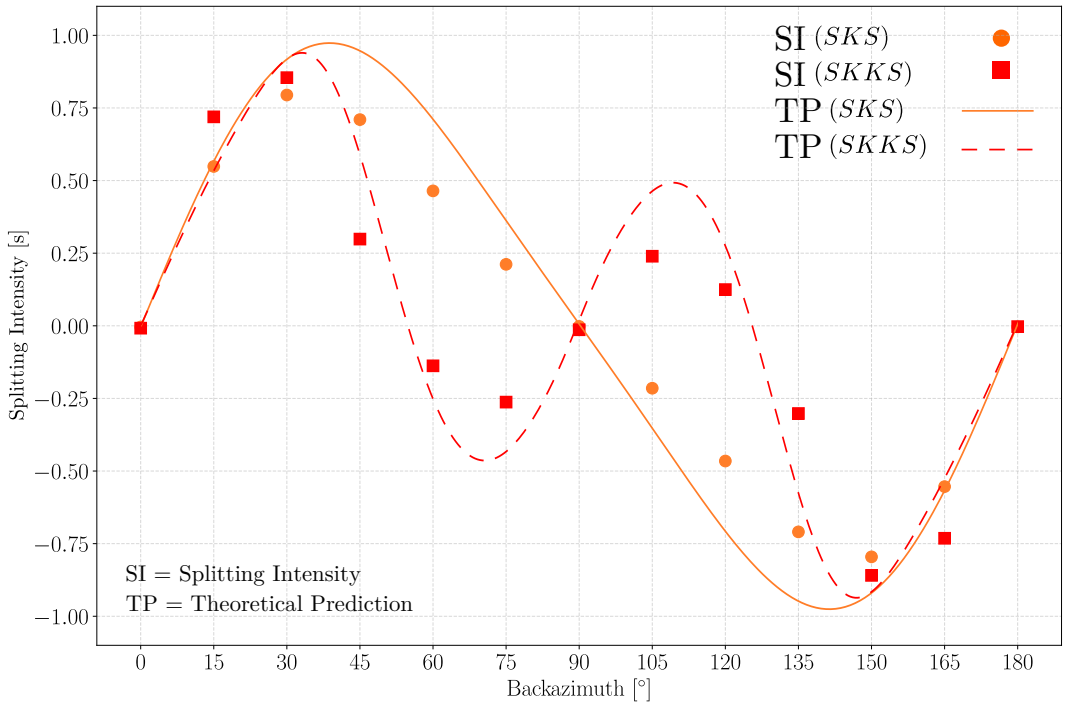

Figure 11. Splitting intensity analysis performed on synthetic seismograms evaluated for the PREM model with anisotropy localized at the base of the lower mantle in a $250km$ thick D'' layer. The elasticity tensor is composed of a linear mixture of 30% bridgmanite from Wookey et al. (2005b) and 70% isotropic PREM (see Figure 4, fourth row). The splitting intensities for SKS (orange circles) and $SKKS$ (red squares) are similar for some specific backazimuth propagation ($0°$ to $30°$ and $150°$ and $180°$) but show discrepancies between $45°$ and $135°$.

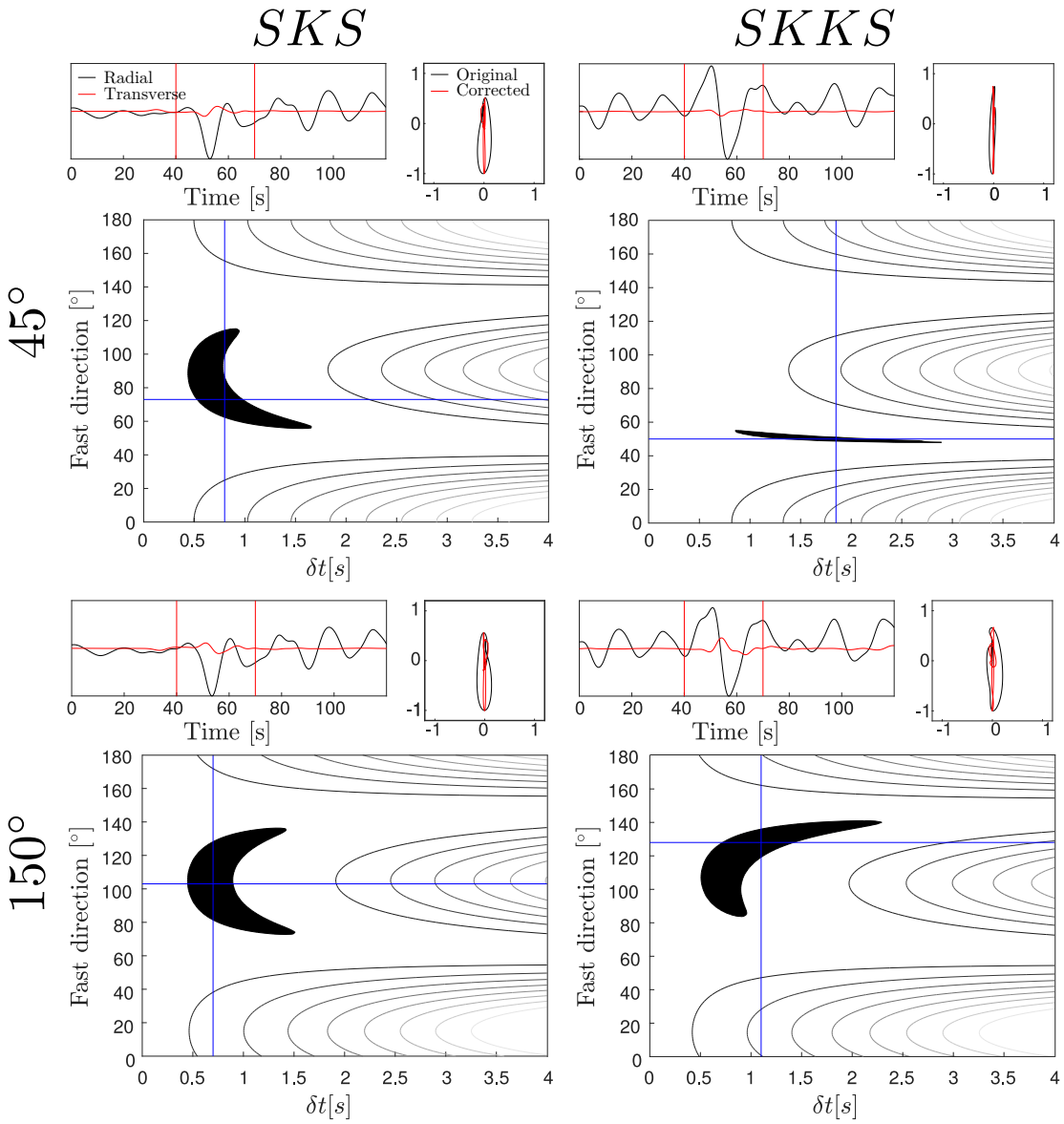

Figure 12. Same analysis presented in Figure 8 but with orthorhombic style anisotropy in the form of a bridgmanite crystal localized in a $250km$ thick D'' layer. As for the splitting intensity analysis, we can see a similar result for SKS and $SKKS$ in the case of seismic energy coming from $150°$ backazimuthal direction and discrepant results for $45°$. We caution, however, that for the $45°$ backazimuth the $SKKS$ splitting measurement is not well constrained.

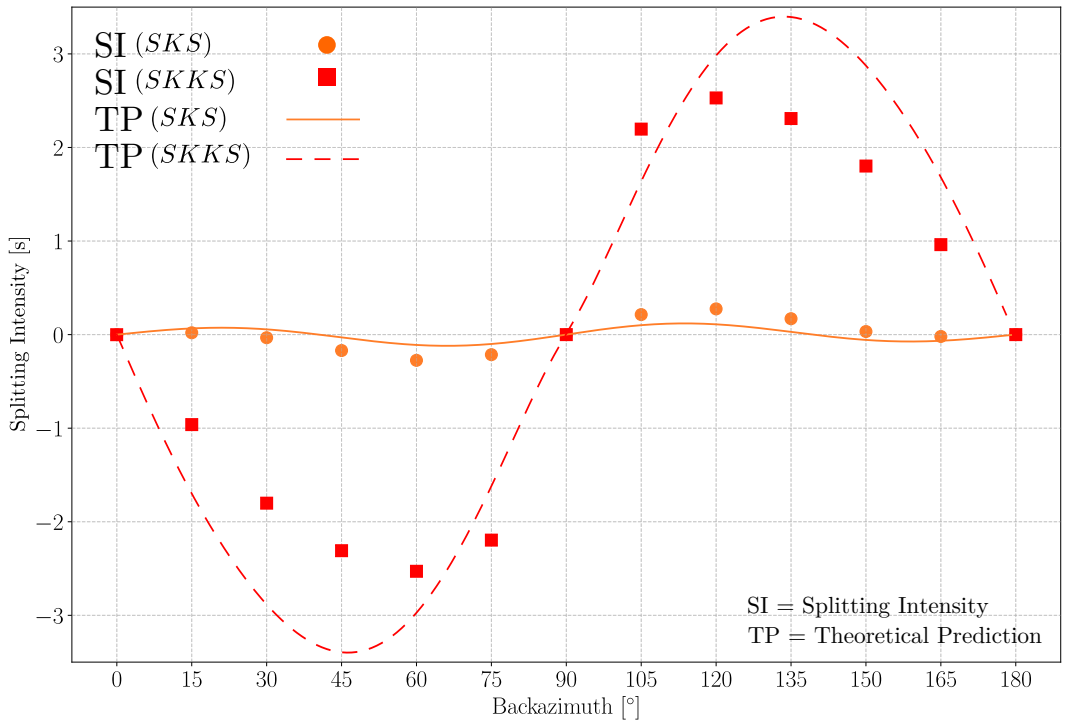

Figure 13. Same as Figure 11 but with an elasticity tensor describing a post-perovskite mineralogy (see Figure 4, bottom row). Strong discrepancies between SKS and $SKKS$ are observed in this case for all the backazimuthal propagation directions with a very strong splitting observed for the $SKKS$ and no splitting (null measurement) observed for the SKS.

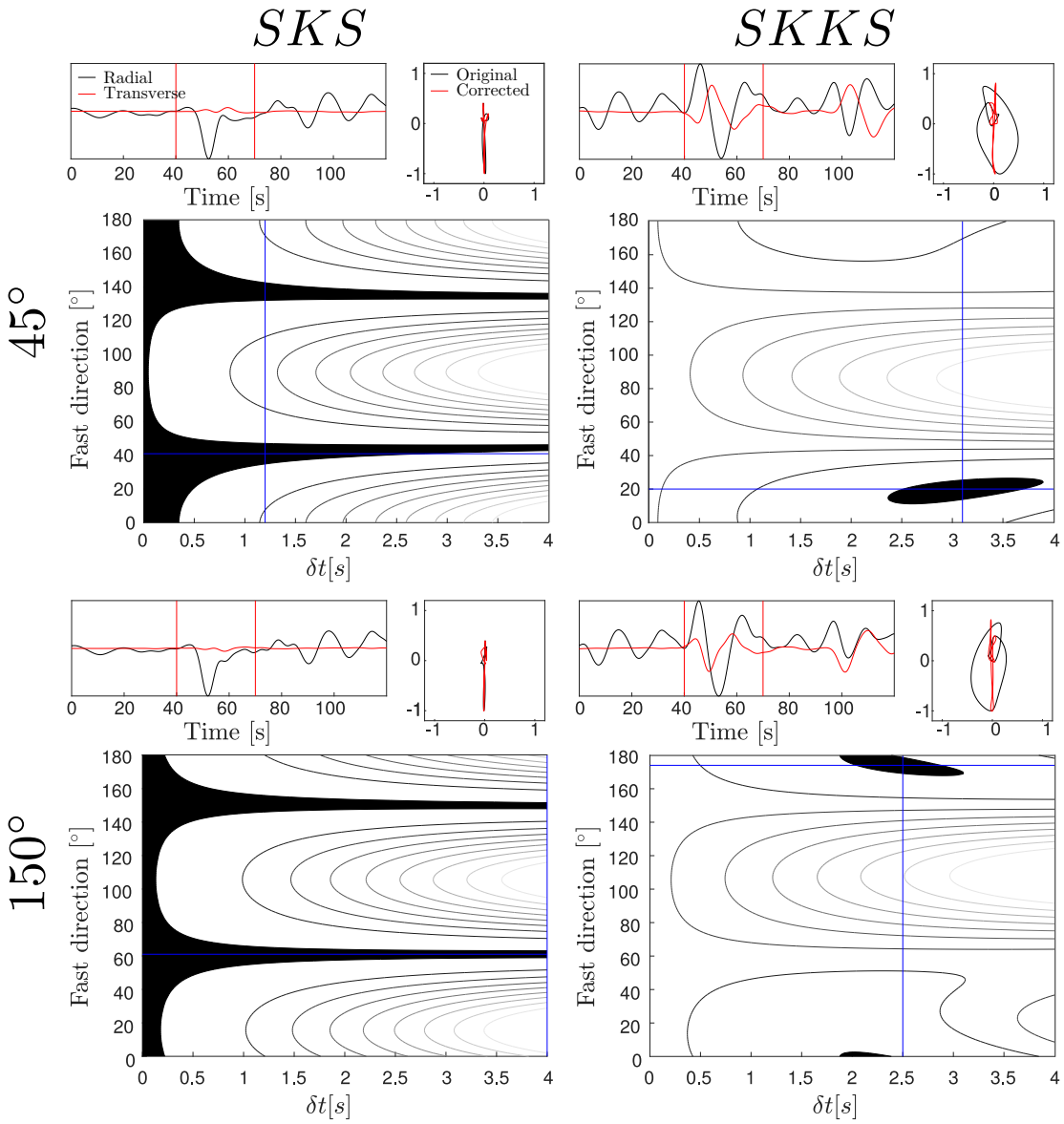

Figure 14. Same as Figure 8 but with the anisotropy localized in a $250km$ thick D'' layer. The elasticity tensor used for this test is the one shown in Fig. 4, bottom row. Also in this case we notice a strong discrepancies between SKS and $SKKS$, with the SKS yielding null measurements.

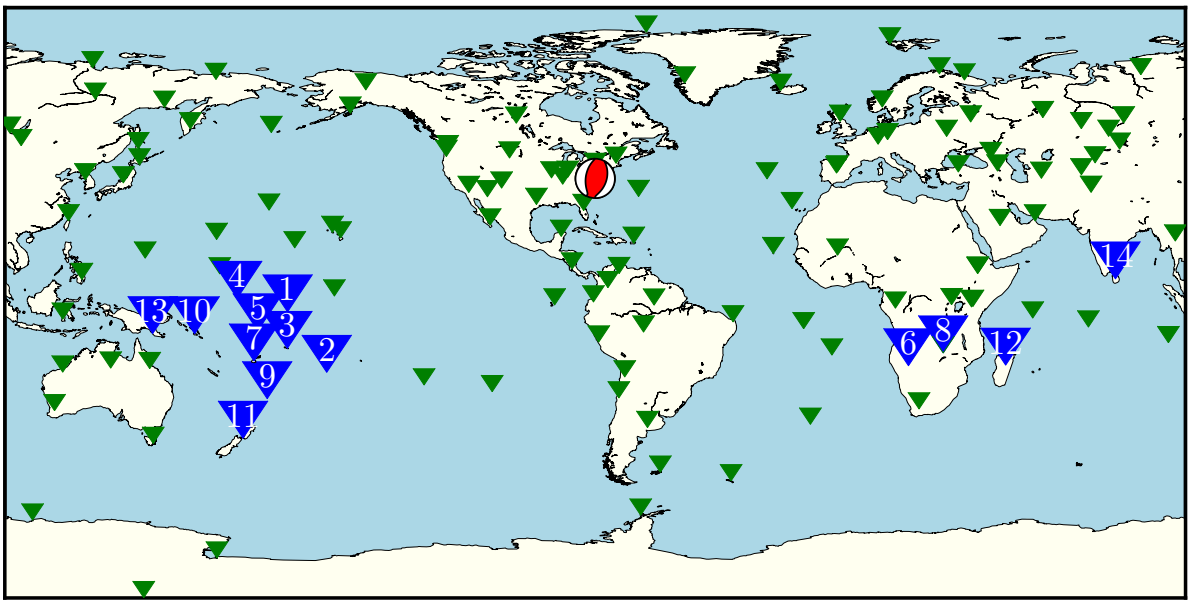

Figure 15. Source and receiver configuration for the AxiSEM3D-SPECFEM3D_GLOBE cross-verification exercise. The earthquake source is located in Virginia, US (37.91°N, 77.93°W), at a depth of $12km$ (event ID 201108231751A). Receivers of the Global Seismographic Network (GSN) are shown as green triangles. The large blue triangles with numbers are 14 representative stations where the synthetic seismograms displayed in Figure 16 are computed.

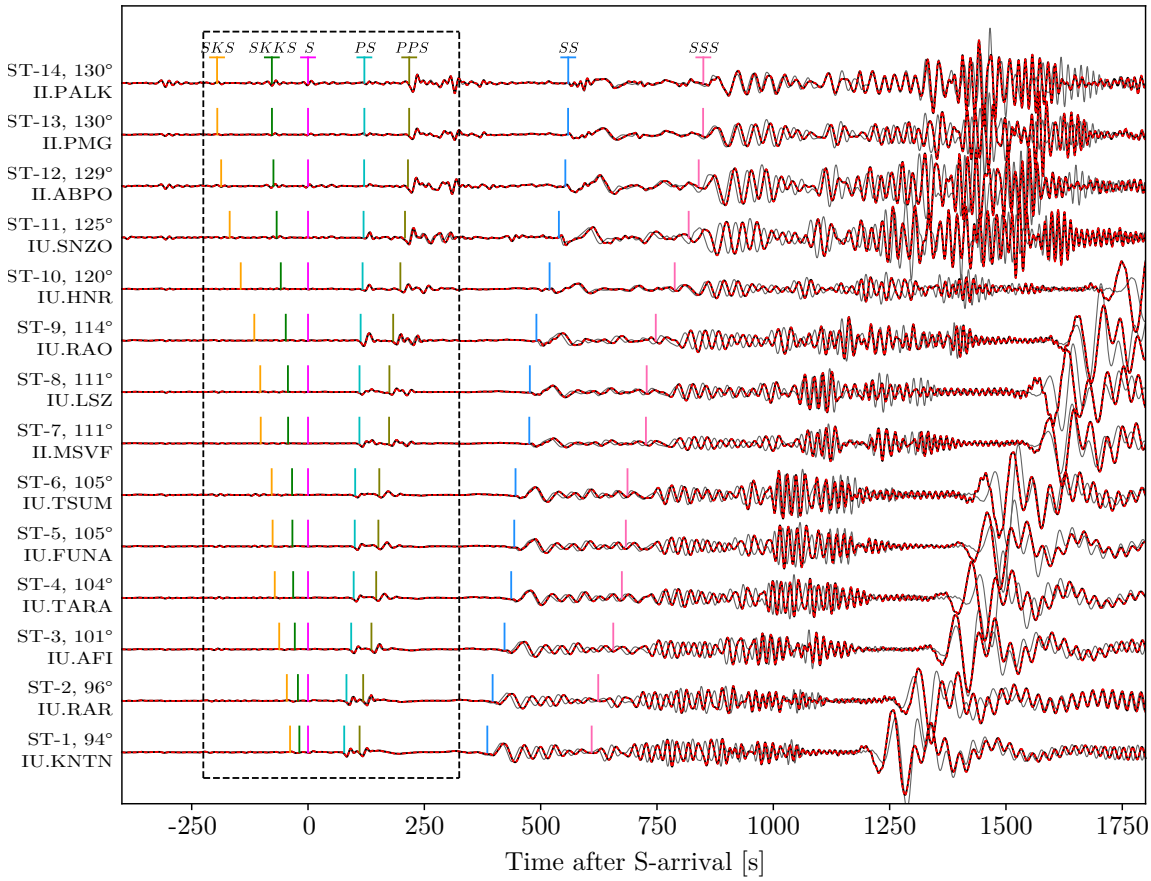

Figure 16. Comparison of synthetic waveforms computed by SPECFEM3D_GLOBE (black) and AxiSEM3D (dashed red) for the tomographic model of Montagner (2002), which includes 3D anisotropy. Synthetic seismograms for the radially anisotropic PREM model are shown in light grey for comparison. We show vertical displacements for all three cases. The receiver locations are shown with blue triangles in Figure 15. Radial and transverse components are shown in Figure 17 in the time-window bounded by the dashed black line that includes SKS and $SKKS$ phases.

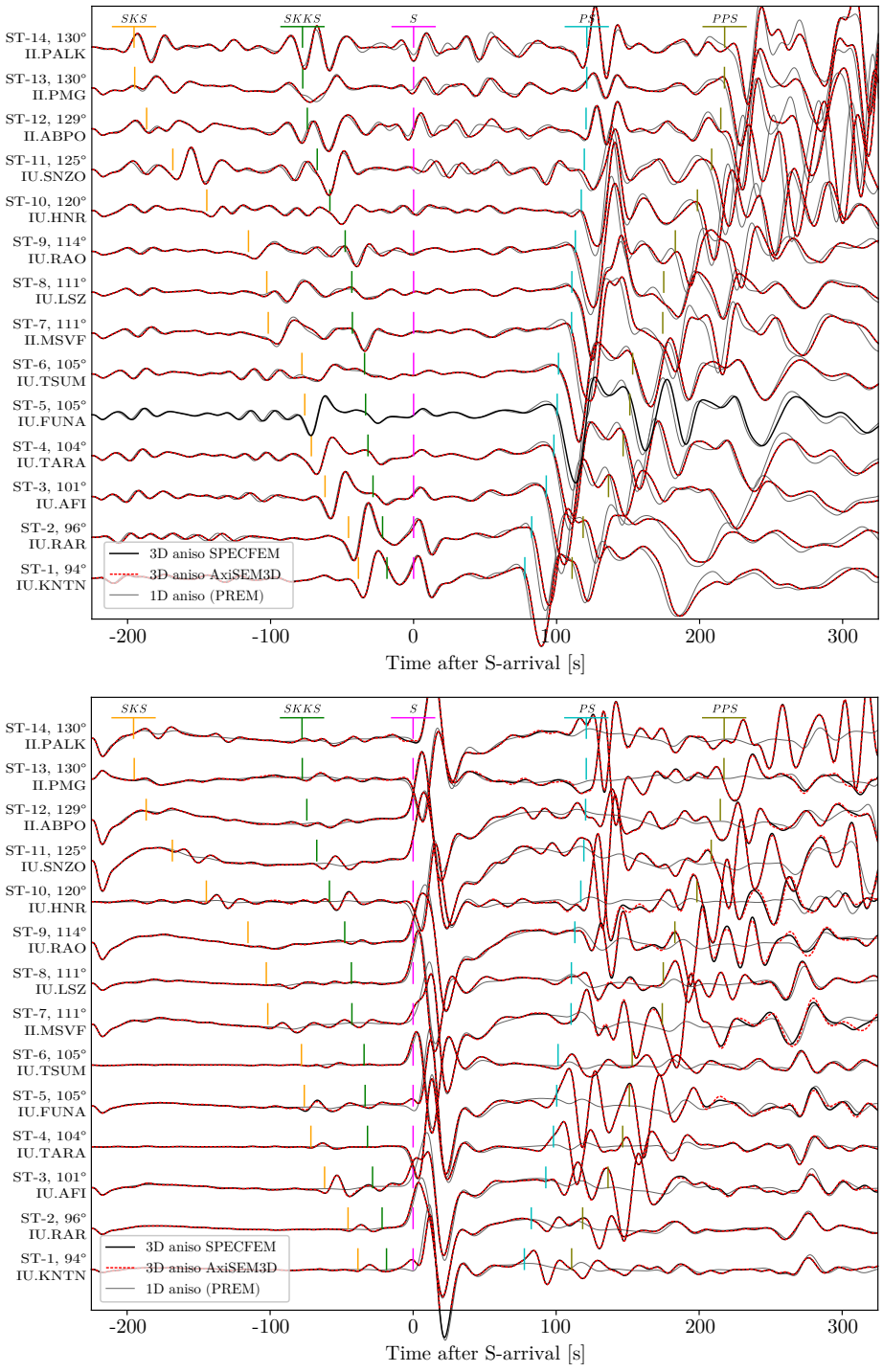

Figure 17. Details of the radial (top panel) and transverse (bottom panel) components of the synthetic waveforms presented in Figure 16. Both AxiSEM3D (dashed red) and SPECFEM3D_GLOBE (black) waveforms show clear evidence of splitting energy between radial and transverse components as a function of the back-azimuth.

submitted to *Geophys. J. Int.*

SI: Full wave sensitivity of $SK(K)S$ phases to arbitrary anisotropy in the upper and lower mantle

Andrea Tesoniero[1], Kuangdai Leng[1,2], Maureen Long[1], Tarje Nissen-Meyer[2]

[1] *Department of Geology and Geophysics, Yale University, 210 Whitney Avenue, New Haven, (CT),* 06520*, USA*

[2] *Department of Earth Sciences, University of Oxford, South Parks Road, Oxford OX1 3AN, UK*

14 March 2020

1 GENERAL INFORMATION

In this supplementary material we present more record section plots showing synthetic seismograms evaluated for the 4 different anisotropic models described in the main text at 3 different epicentral distance (100°, 110° and 120°) and for the AxiSEM3D-SPECFEM3D_GLOBE benchmark test.

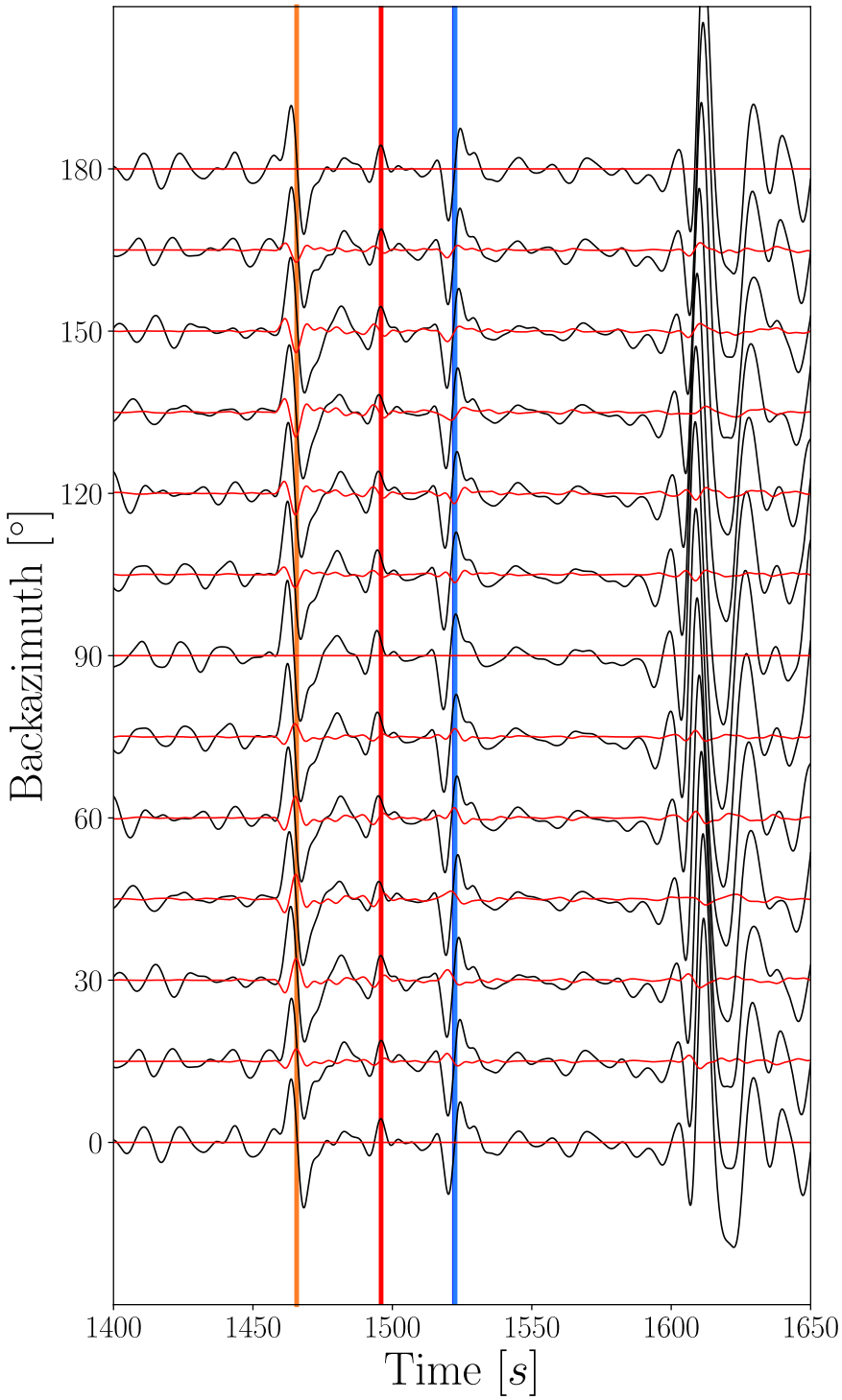

Figure S1. Synthetic seismograms computed for the PREM model with a HTI layer localized between 24 and $220km$ plotted against the backazimuth of the incoming seismic energy. The epicentral distance is 100°. The radial component is shown in black and the transverse is shown in red. Predicted arrival time for SKS, $SKKS$ and ScS are shown as the vertical orange, red and blue bars respectively.

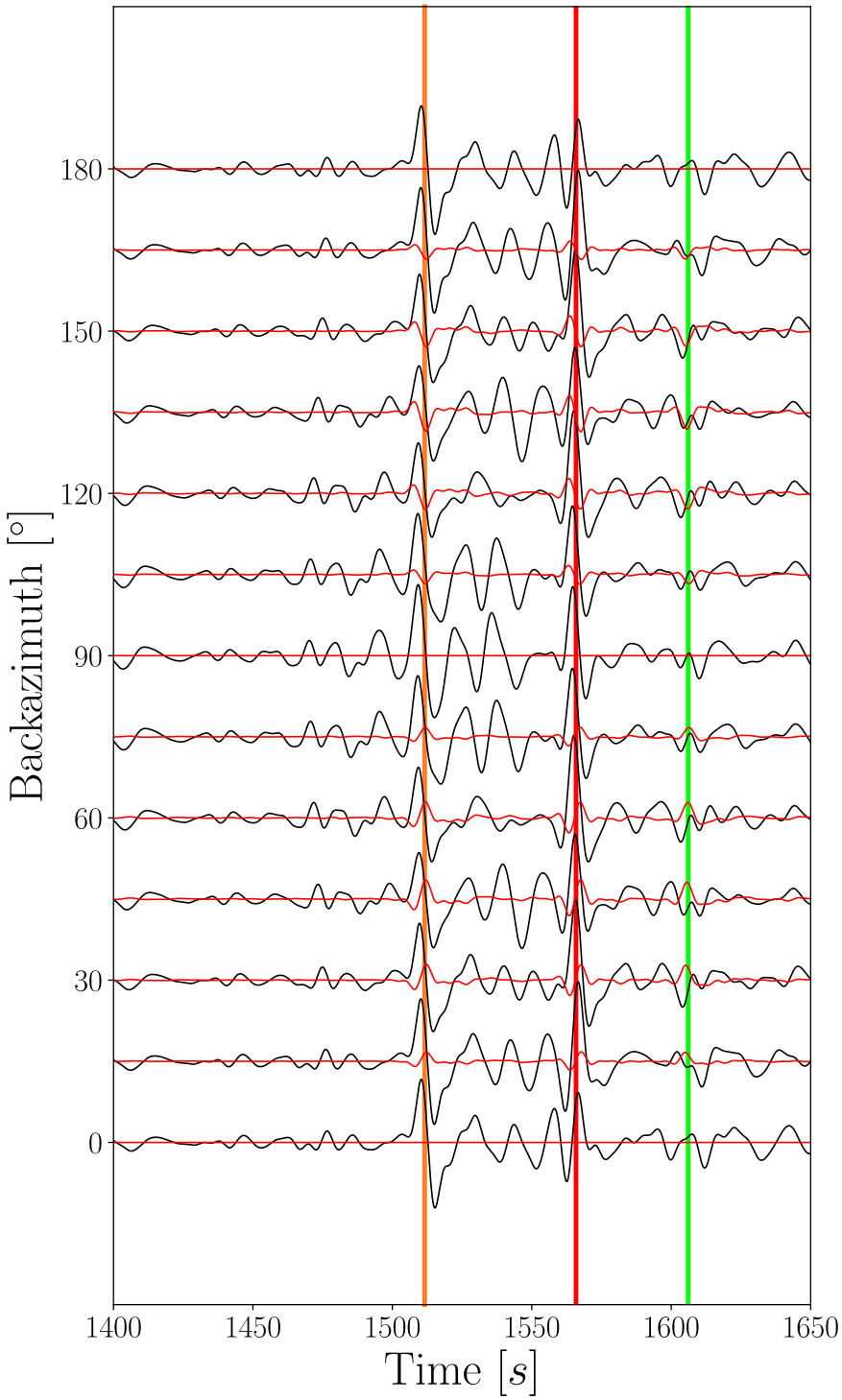

Figure S2. Synthetic seismograms computed for the PREM model with a HTI layer localized between 24 and $220km$ plotted against the backazimuth of the incoming seismic energy. The epicentral distance is $110°$. The radial component is shown in black and the transverse is shown in red. Predicted arrival time for SKS, $SKKS$ and S_{diff} are shown as the vertical orange, red and green bars respectively.

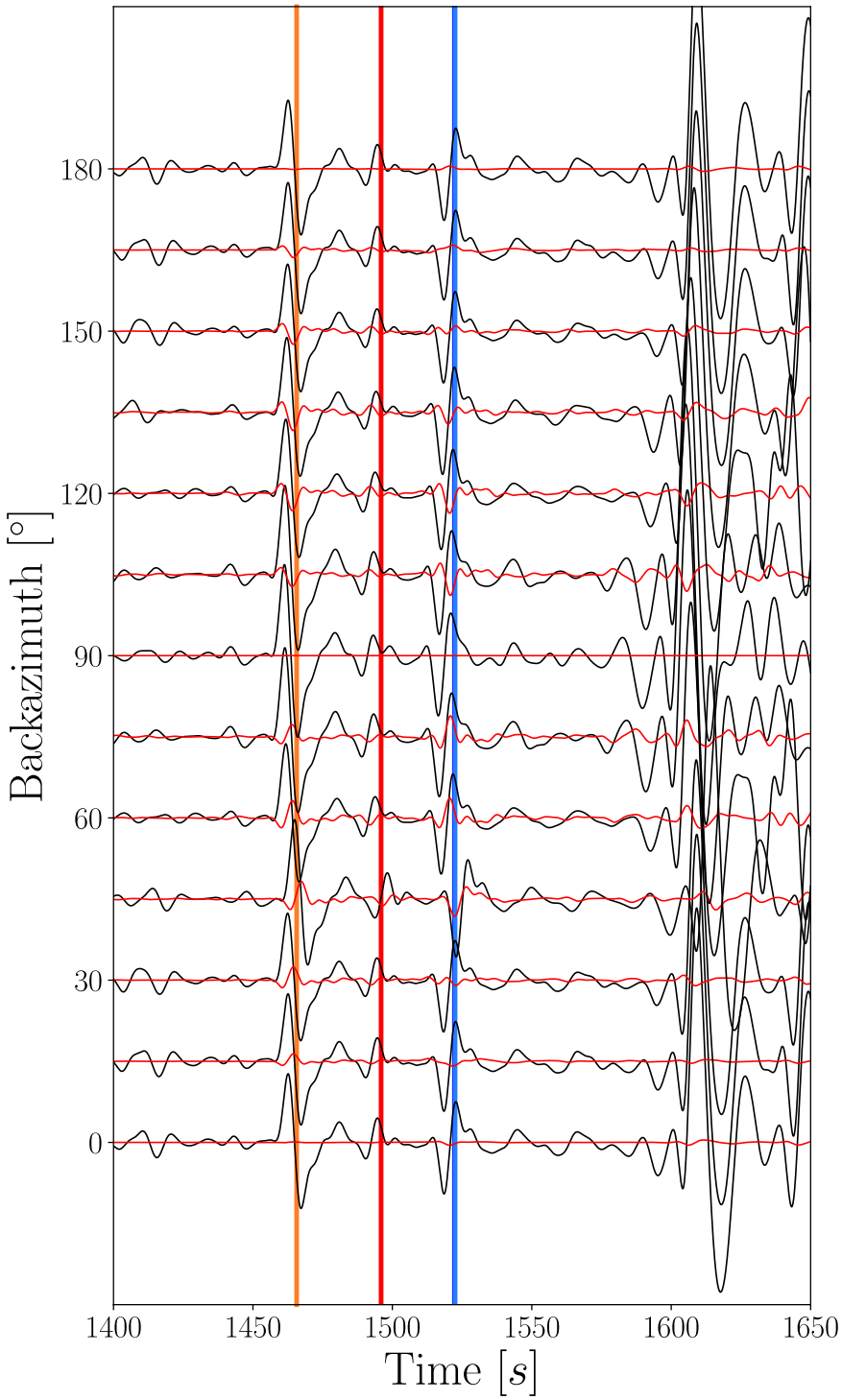

Figure S3. Synthetic seismograms computed for the PREM model with olivine style anisotropy localized between 24 and 220km plotted against the backazimuth of the incoming seismic energy. The epicentral distance is 100°. The radial component is shown in black and the transverse is shown in red. Predicted arrival time for SKS, $SKKS$ and Scs are shown as the vertical orange, red and blue bars respectively.

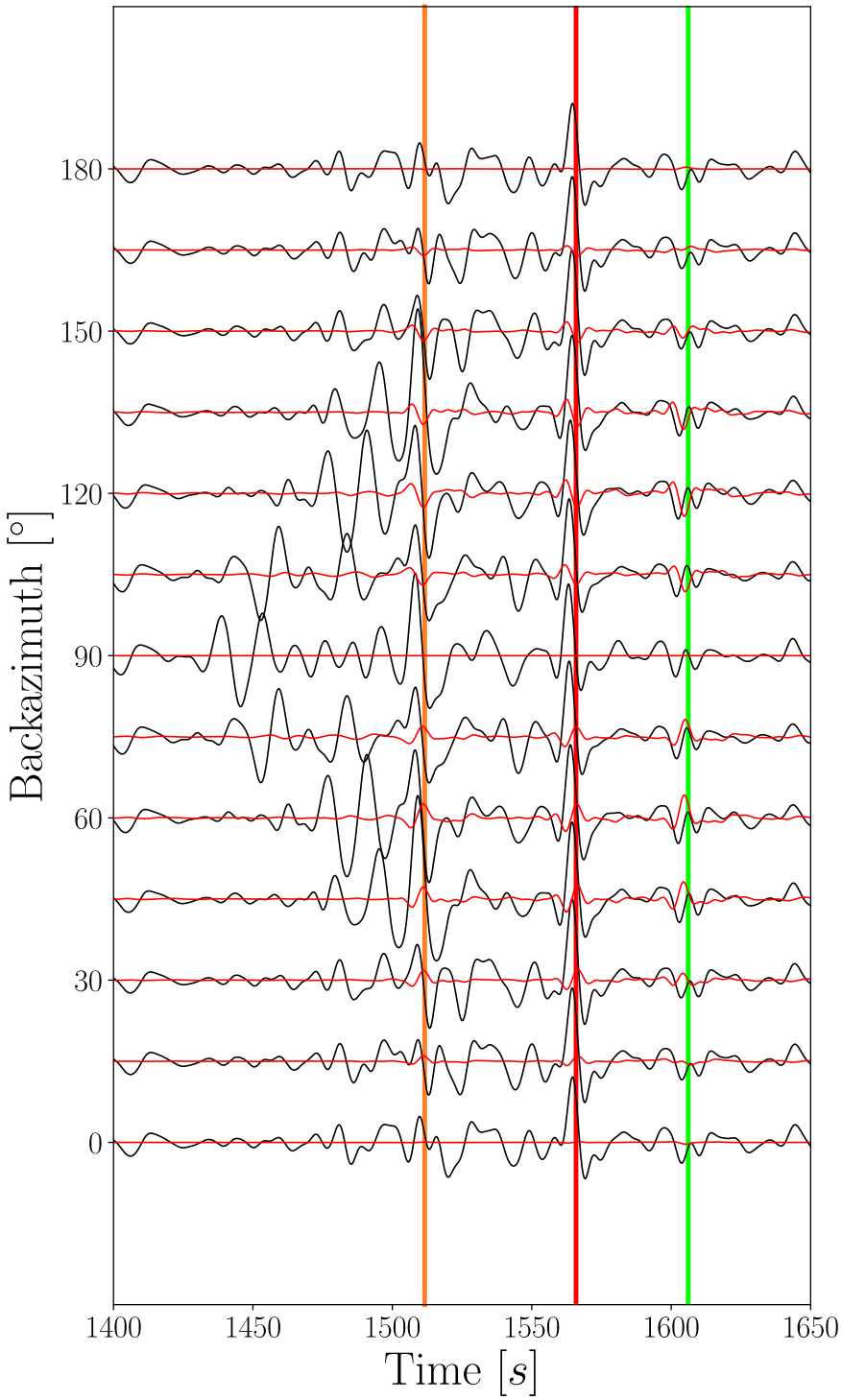

Figure S4. Synthetic seismograms computed for the PREM model with olivine style anisotropy localized between 24 and 220km plotted against the backazimuth of the incoming seismic energy. The epicentral distance is 110°. The radial component is shown in black and the transverse is shown in red. Predicted arrival time for SKS, $SKKS$ and S_{diff} are shown as the vertical orange, red and green bars respectively. Phases with large amplitude arriving in the $1450 - 1500s$ range correspond to $PPPP$. For this particular symmetry class they are strongly affected by the anisotropy in the backazimuthal range $45 - 135°$.

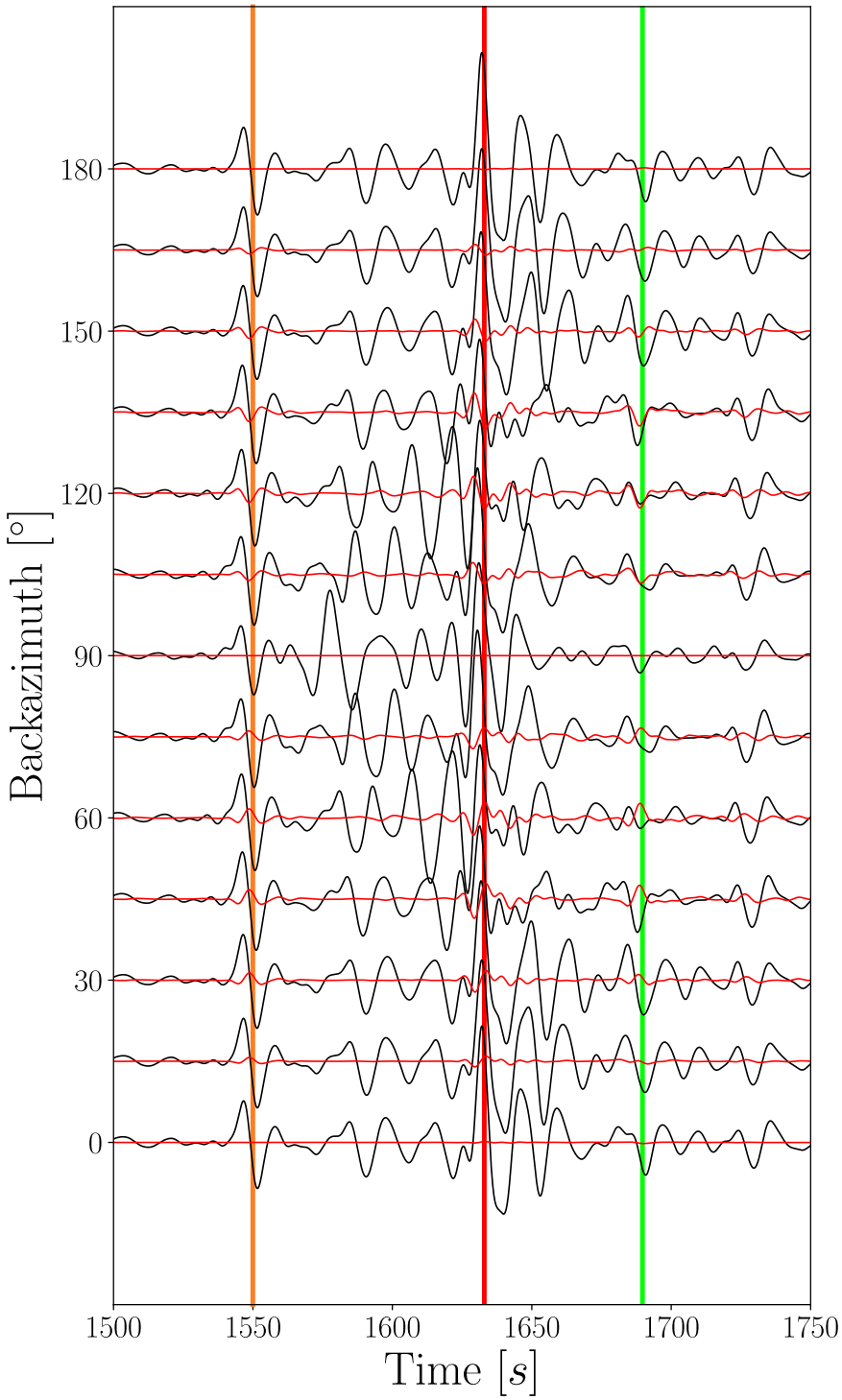

Figure S5. Synthetic seismograms computed for the PREM model with olivine style anisotropy localized between 24 and $220km$ plotted against the backazimuth of the incoming seismic energy. The epicentral distance is $120°$. The radial component is shown in black and the transverse is shown in red. Predicted arrival time for SKS, $SKKS$ and S_{diff} are shown as the vertical orange, red and green bars respectively. Phases with large amplitude arriving between SKS ans $SKKS$ correspond to $PPPP$. For this particular symmetry class they are strongly affected by the anisotropy in the backazimuthal range $45 - 135°$.

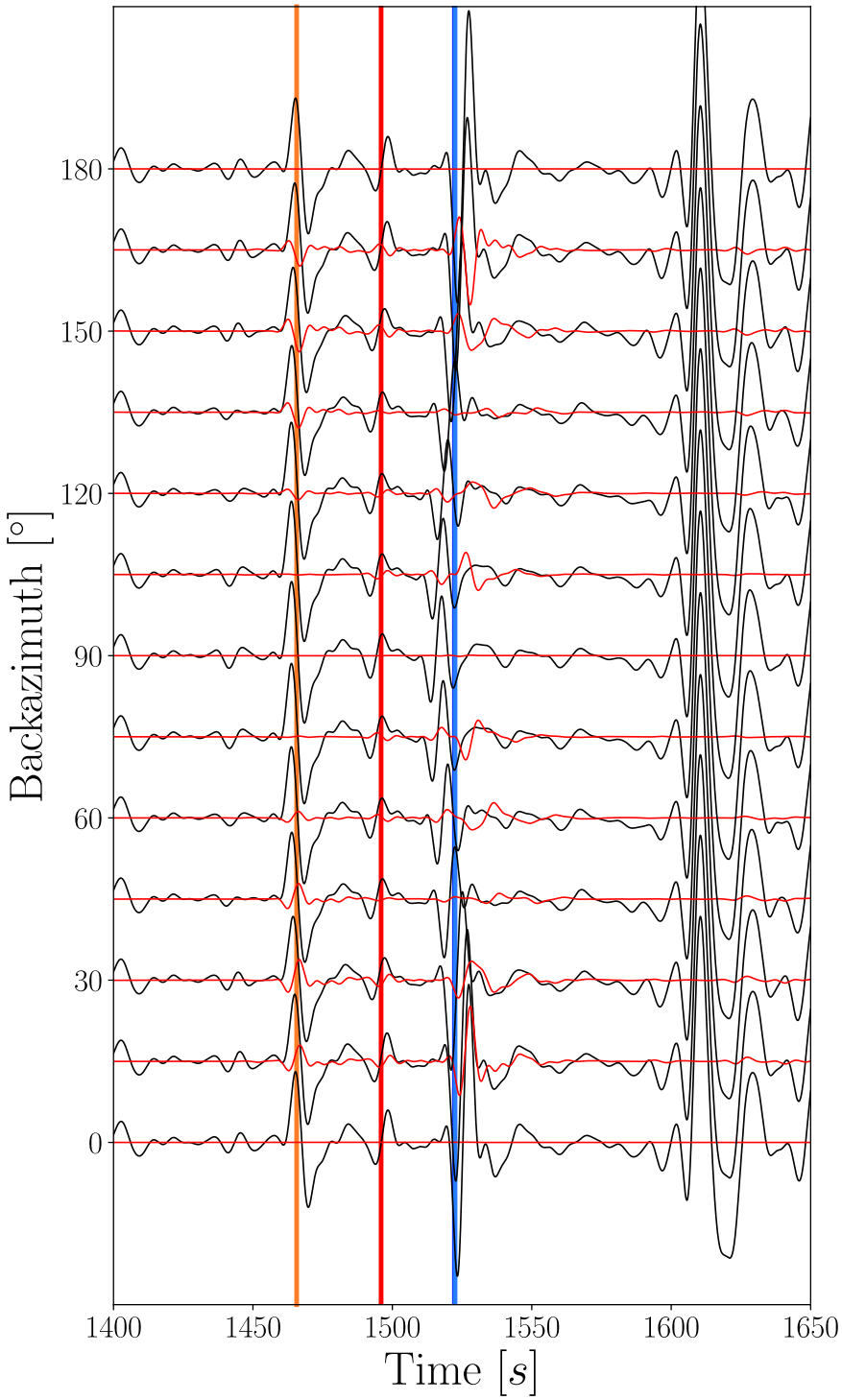

Figure S6. Synthetic seismograms computed for the PREM model bridgmanite style anisotropy localized at the base of the base of the lower mantle in a $250km$ thick D'' plotted against the backazimuth of the incoming seismic energy. The epicentral distance is 100°. The radial component is shown in black and the transverse is shown in red. Predicted arrival time for SKS, $SKKS$ and ScS are shown as the vertical orange, red and blue bars respectively.

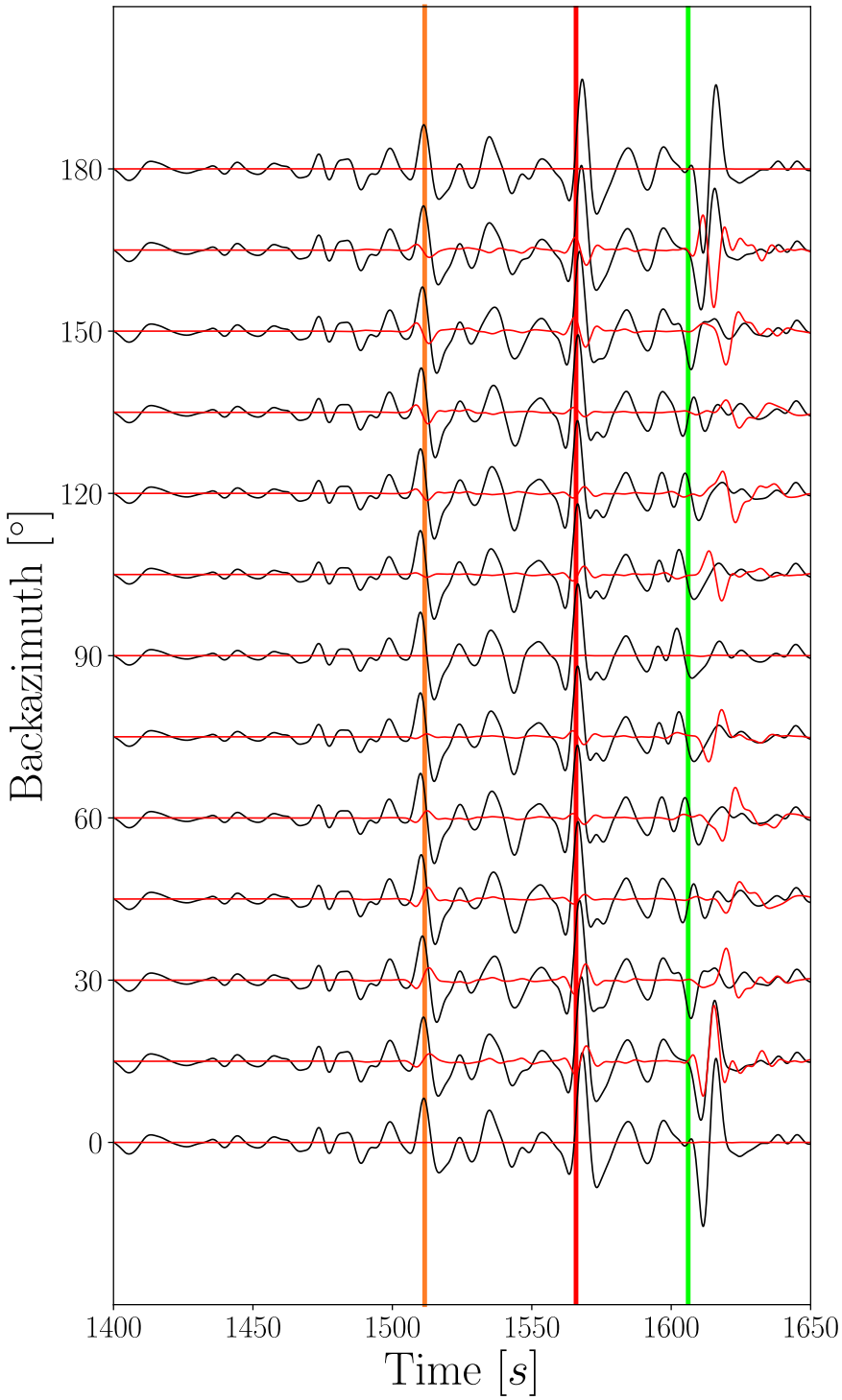

Figure S7. Synthetic seismograms computed for the PREM model a bridgmanite style anisotropy localized at the base of the base of the lower mantle in a $250km$ thick D'' plotted against the backazimuth of the incoming seismic energy. The epicentral distance is 110°. The radial component is shown in black and the transverse is shown in red. Predicted arrival time for SKS, $SKKS$ and S_{diff} are shown as the vertical orange, red and green respectively.

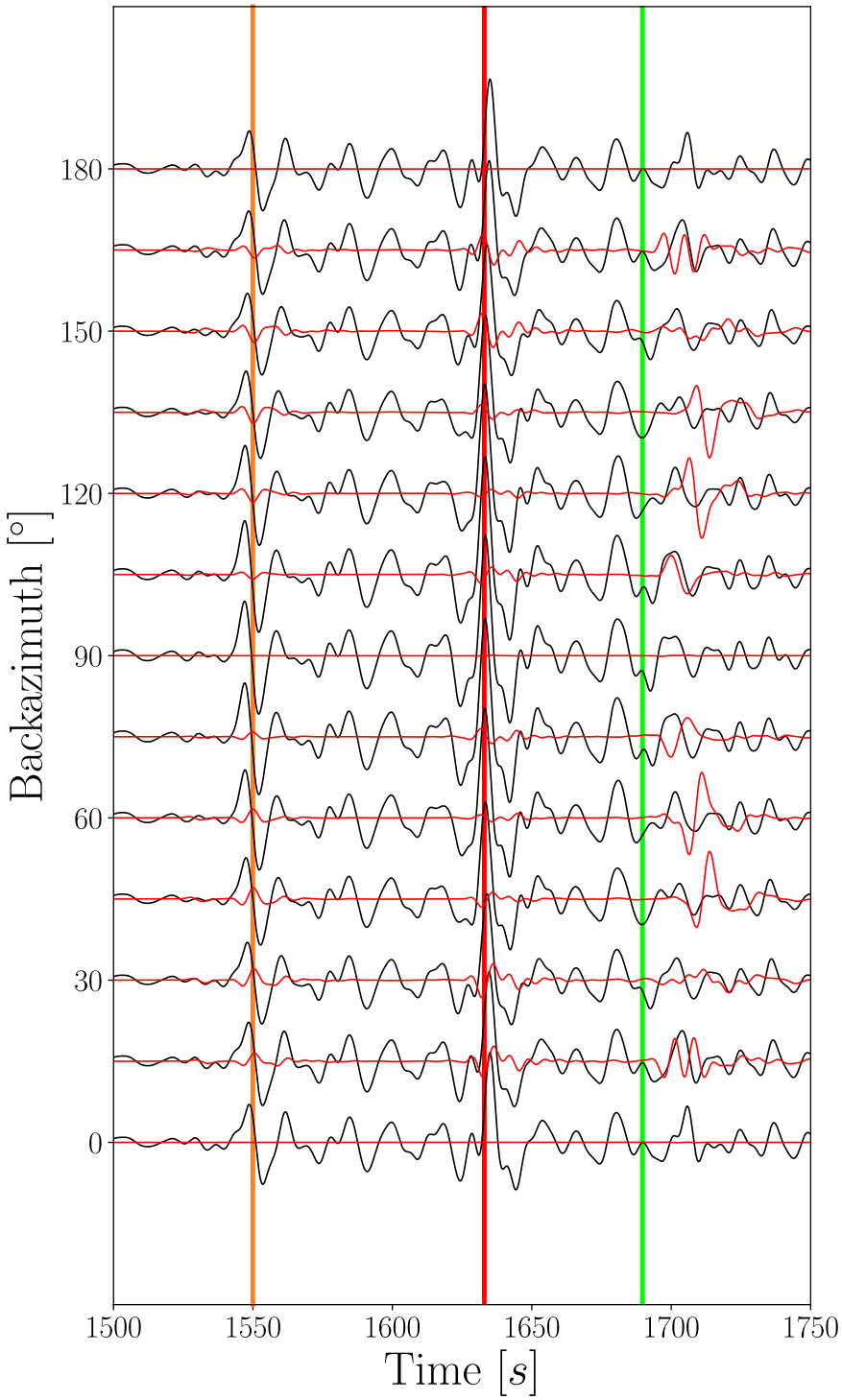

Figure S8. Synthetic seismograms computed for the PREM model bridgmanite style anisotropy localized at the base of the base of the lower mantle in a $250km$ thick D'' plotted against the backazimuth of the incoming seismic energy. The epicentral distance is 120°. The radial component is shown in black and the transverse is shown in red. Predicted arrival time for SKS, $SKKS$ and S_{diff} are shown as the vertical orange, red and green respectively.

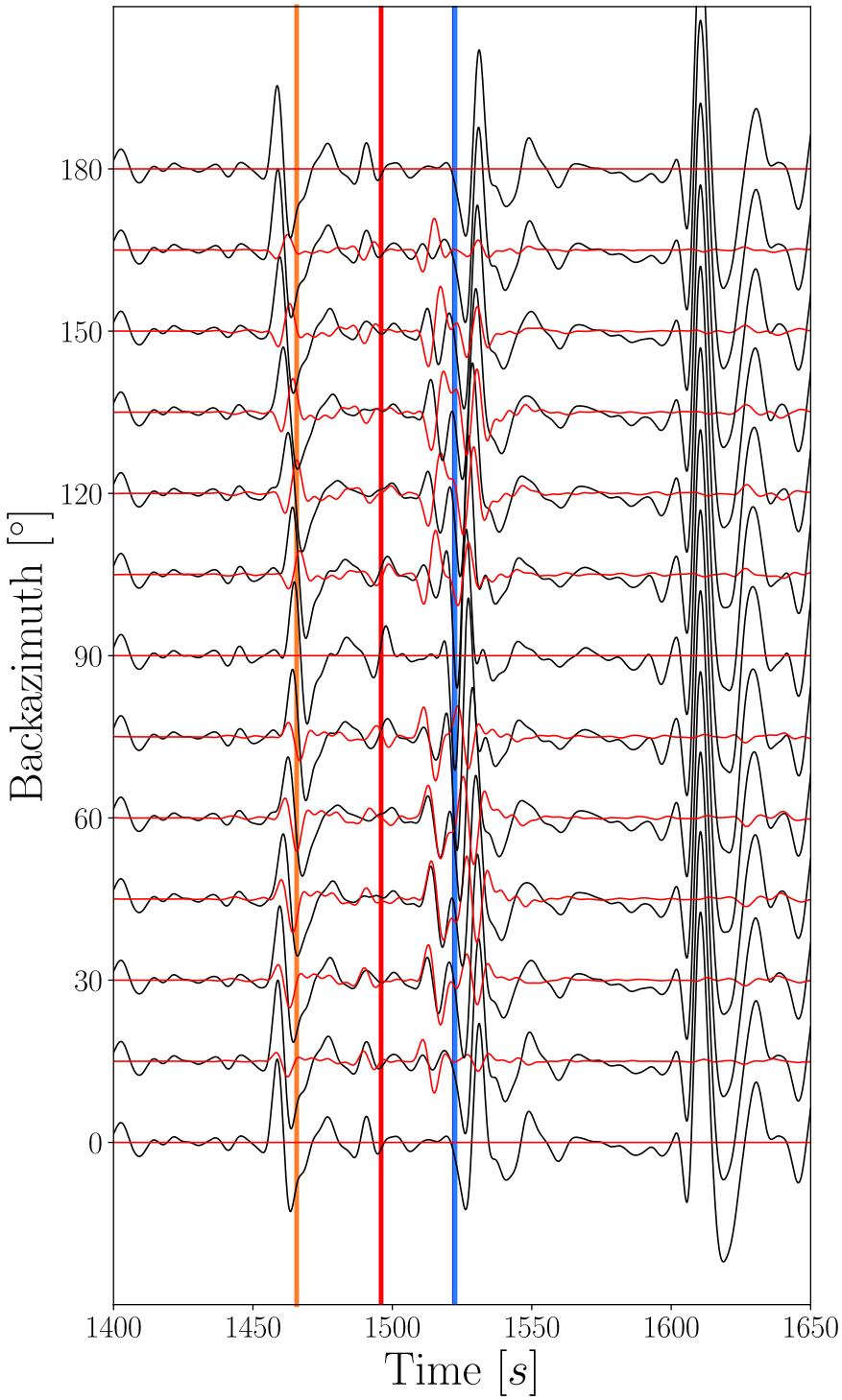

Figure S9. Synthetic seismograms computed for the PREM model with post-perovskite style anisotropy localized at the base of the base of the lower mantle in a $250km$ thick D'' plotted against the backazimuth of the incoming seismic energy. The epicentral distance is $100°$. The radial component is shown in black and the transverse is shown in red. Predicted arrival time for SKS, $SKKS$ and ScS are shown as the vertical orange, red and blue respectively.

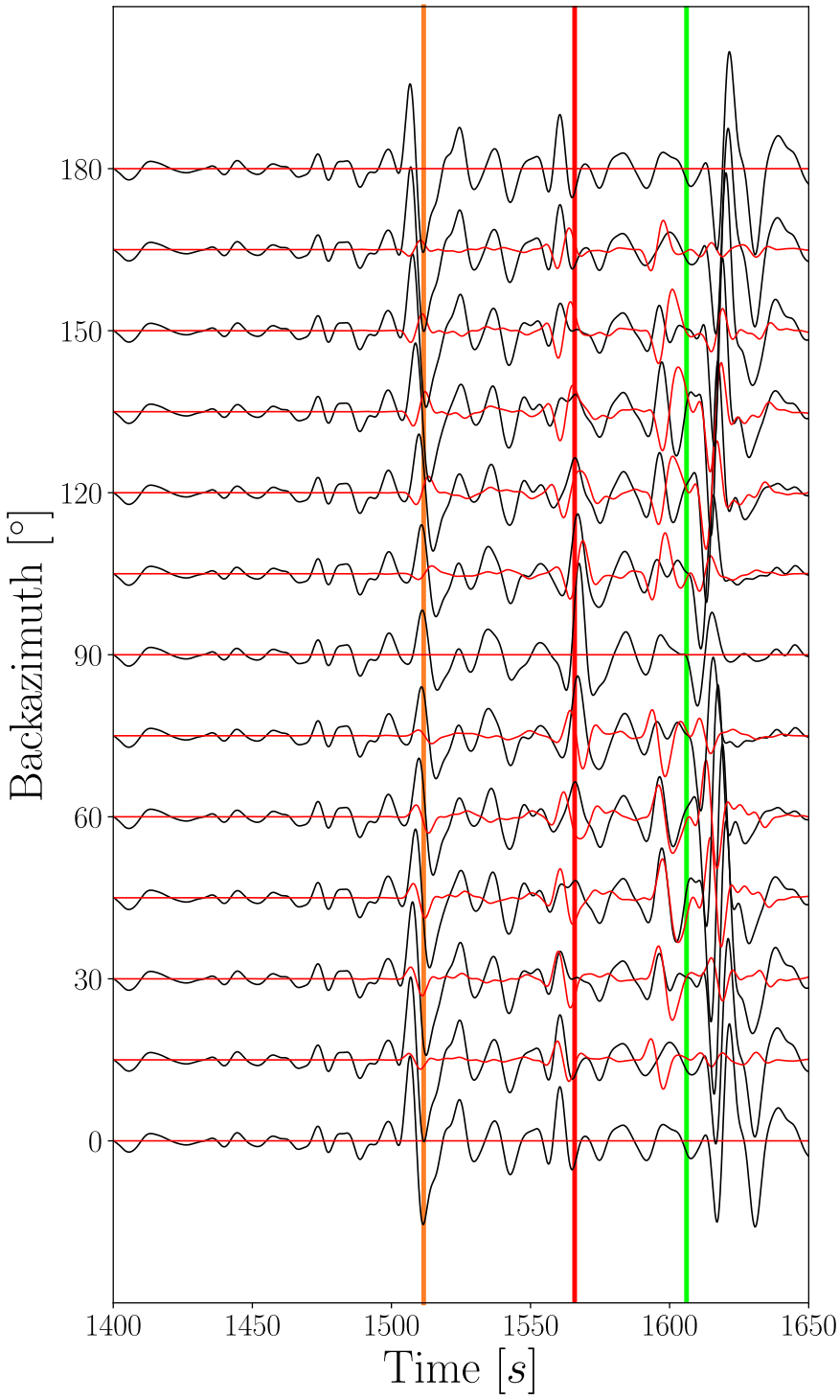

Figure S10. Synthetic seismograms computed for the PREM model with post-perovskite style anisotropy localized at the base of the base of the lower mantle in a $250km$ thick D'' plotted against the backazimuth of the incoming seismic energy. The epicentral distance is $110°$. The radial component is shown in black and the transverse is shown in red. Predicted arrival time for SKS, $SKKS$ and S_{diff} are shown as the vertical orange, red and green respectively.

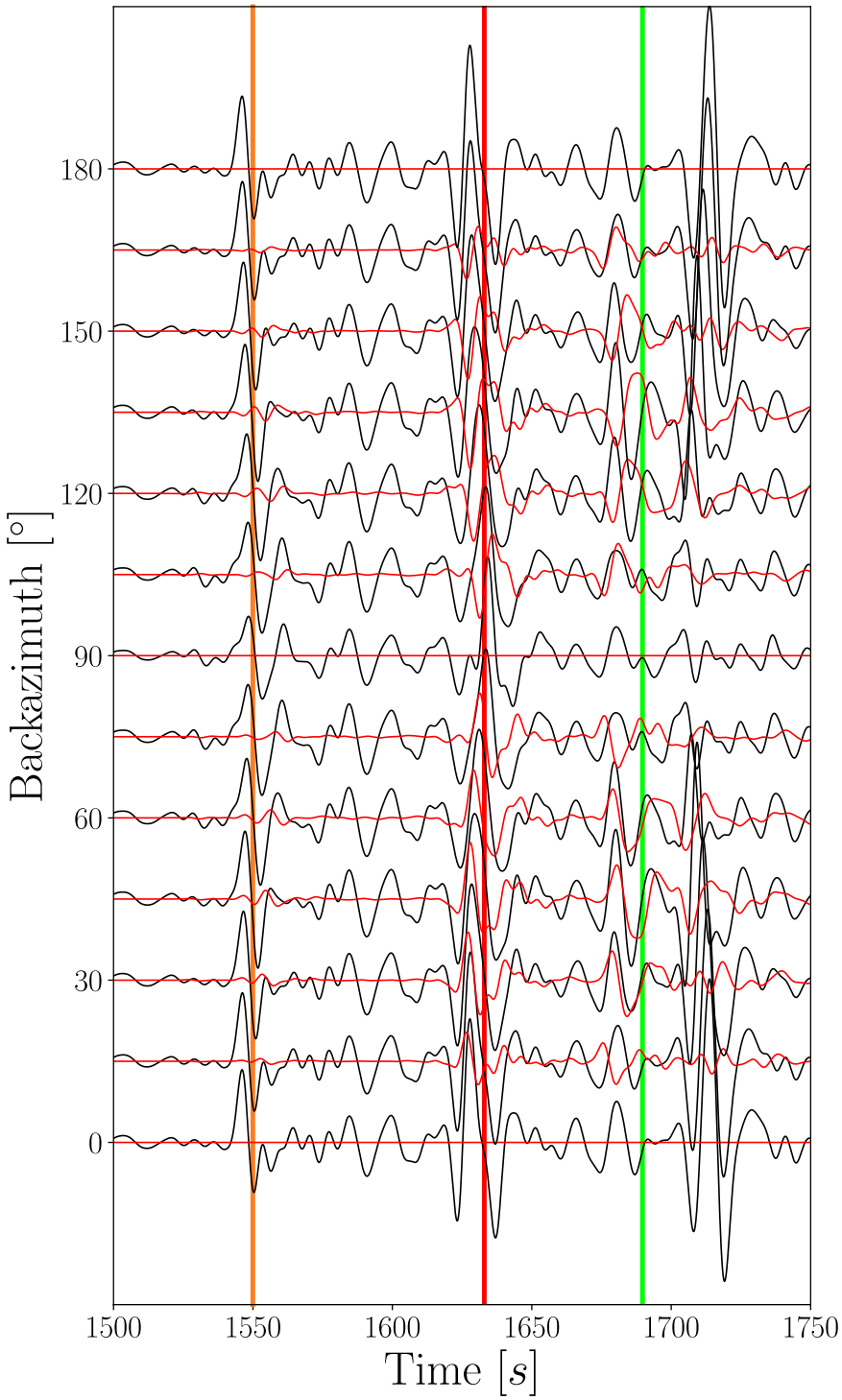

Figure S11. Synthetic seismograms computed for the PREM model with post-perovskite style anisotropy localized at the base of the base of the lower mantle in a $250km$ thick D'' plotted against the backazimuth of the incoming seismic energy. The epicentral distance is 120°. The radial component is shown in black and the transverse is shown in red. Predicted arrival time for SKS, $SKKS$ and S_{diff} are shown as the vertical orange, red and green respectively.

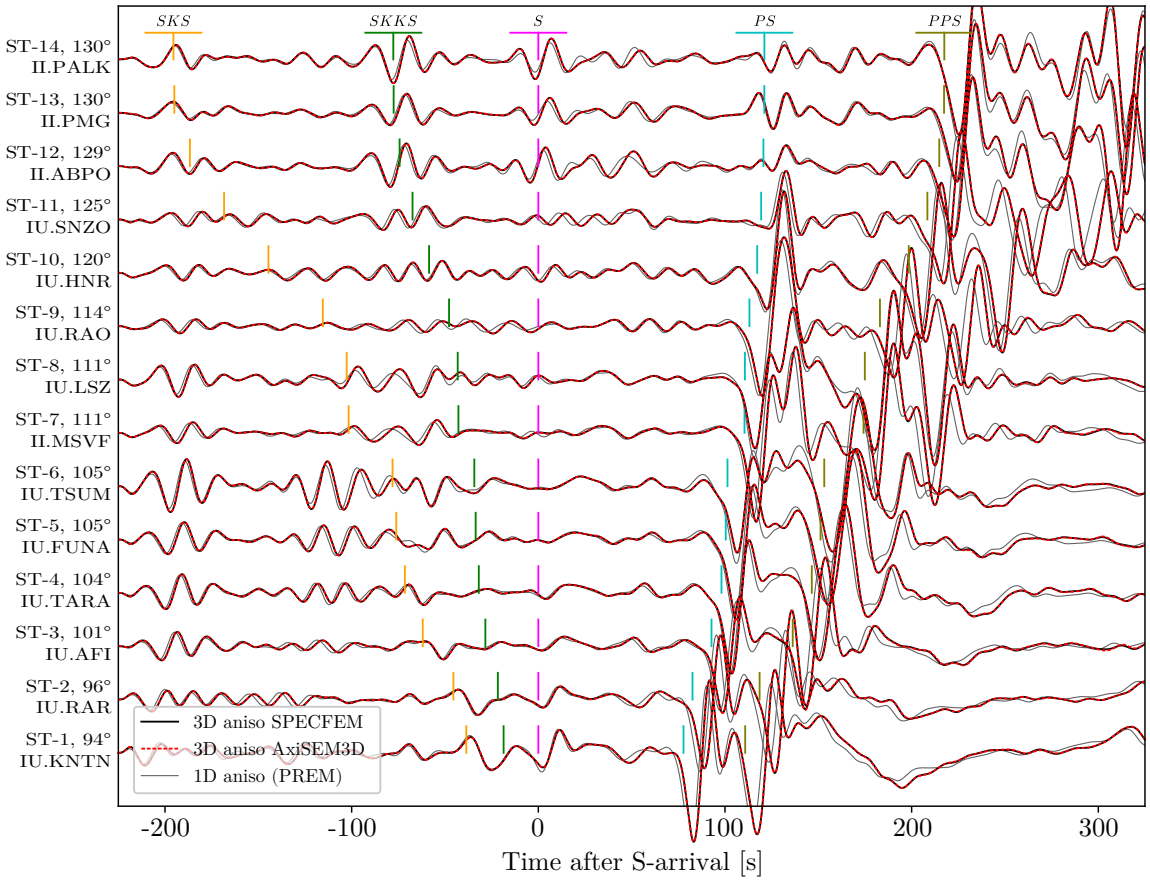

Figure S12. Same as Figure 17 of the main manuscript but for the vertical component.

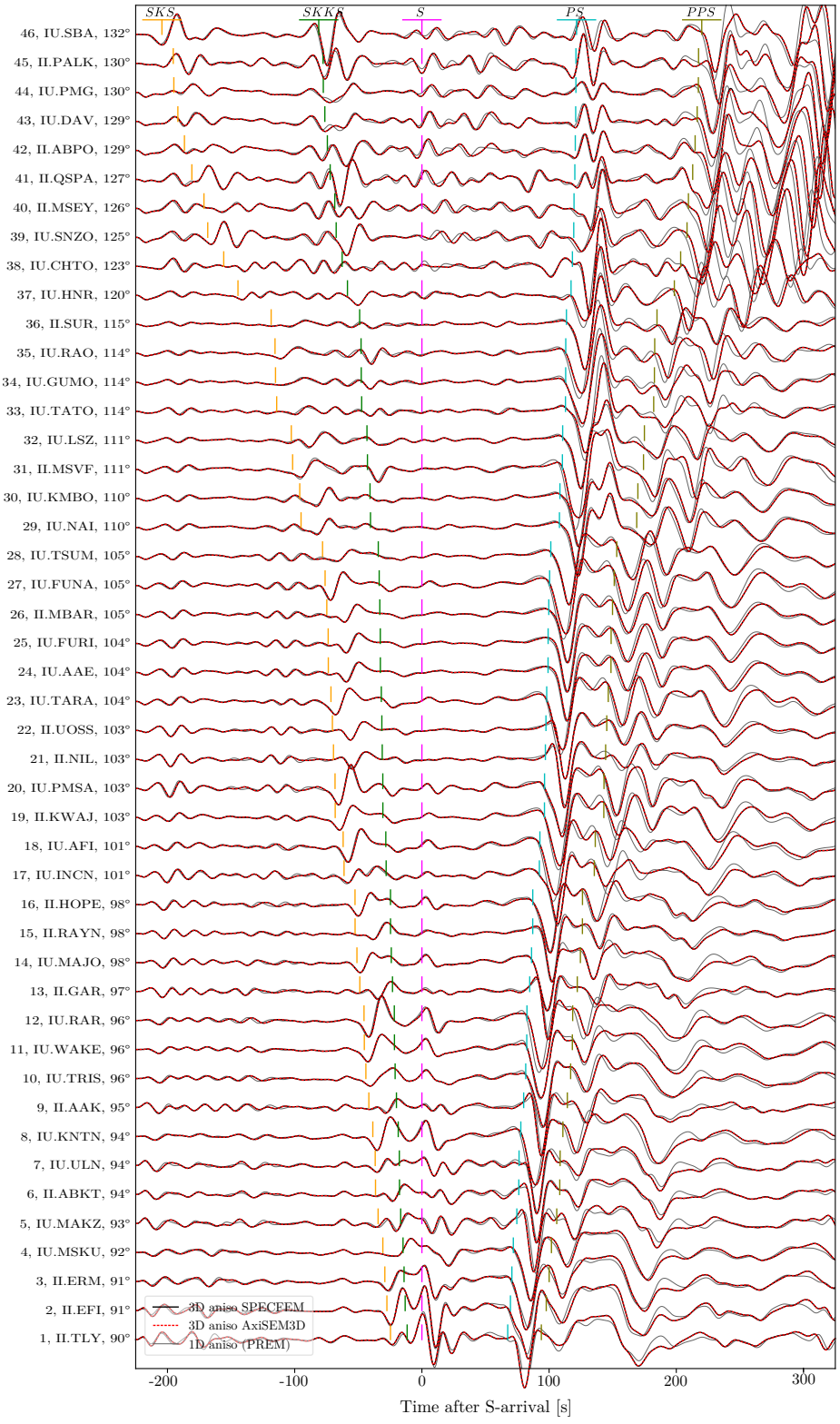

Figure S13. Comparison of synthetic waveforms computed by SPECFEM3D_GLOBE (black) and AxiSEM3D (dashed red) for the benchmark test presented in Section 6 of the main text. The record section shows the radial component for all the stations mapped in Figure 15 of the main text located in the $\sim 90° - 130°$ range of epicentral distance.

Figure S14. Same as Figure S13 but for the transverse component.

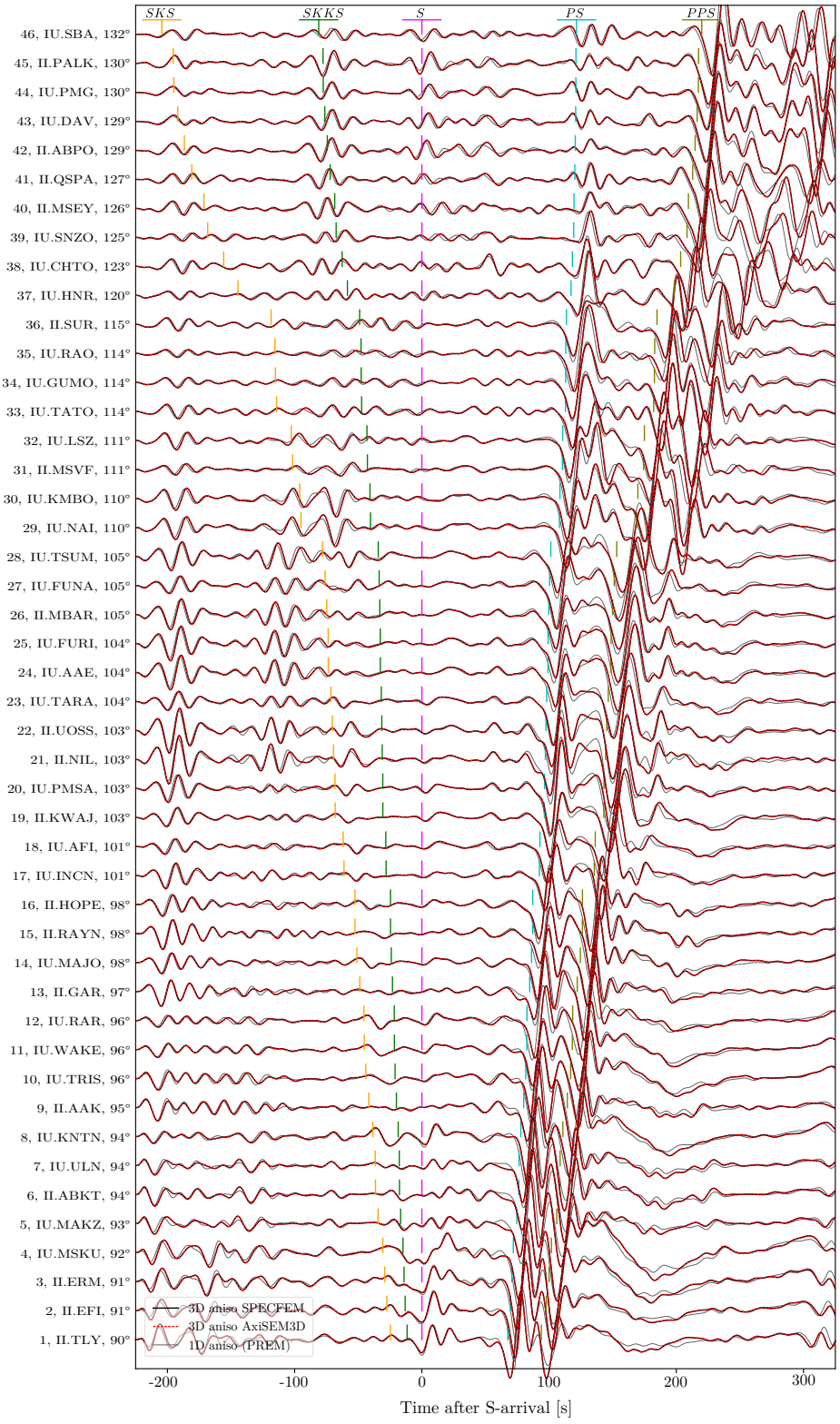

Figure S15. Same as Figure S13 but for the vertical component.